Escape from the HER2-activated DCIS-like state is skewed by divergent nucleocytoplasmic transport

Lixin Wang[1,4], B. Bishal Paudel[1,4], R. Anthony McKnight[1,3], Kevin A. Janes[1,2]✉

[1]Department of Biomedical Engineering, University of Virginia, Charlottesville, Virginia, USA.
[2]Department of Biochemistry & Molecular Genetics, University of Virginia, Charlottesville, Virginia, USA.
[3]Present address: Olympus Veran Technologies, St. Louis, Missouri, USA.
[4]These authors contributed equally: L. Wang, B.B. Paudel.

✉Email: kjanes@virginia.edu

ABSTRACT

Activation of ErbB receptors—HER2/ErbB2 and EGFR/ErbB1—disrupts 3D multicellular organization of breast-epithelial cells with characteristics resembling premalignant escape from ductal carcinoma in situ (DCIS). However, the escape phenotype is infrequent, and a mechanism for its incomplete penetrance has been elusive. By matching phenotype penetrance to the frequency of transcriptomic fluctuations that co-occur, we uncovered a karyopherin network regulating nucleocytoplasmic transport of ErbBs. The exportin CSE1L is sporadically induced and inhibits nuclear accumulation of ErbBs. Separately, nuclear ErbBs upregulate miR-205 to repress protein abundance of the importin KPNA1. When these feedbacks are incorporated into a validated systems model of nucleocytoplasmic transport, steady-state localization of ErbB cargo becomes ultrasensitive to the concentration of CSE1L. Variations or cancer-associated mutations in the NLS-like sequence of HER2 weaken transport and favor the escape phenotype in 3D culture. In vivo, knockdown of Cse1l attenuates the irregular outgrowth of Erbb2-activated mammary carcinomas, suggesting future therapeutic potential.

INTRODUCTION

In breast tissue, focal amplification of *ERBB2* gives rise to constitutive ErbB signaling that is oncogenic[1]. *ERBB2* amplification or upregulation occurs at the premalignant ductal carcinoma in situ (DCIS) stage[2-6], and DCIS lesions adjacent to *ERBB2*-amplified carcinomas almost always show *ERBB2* amplification[6, 7]. However, as an early oncogenic event for noncancerous tissue, *ERBB2* amplification by itself elevates DCIS risk quite modestly[5]. The proportion of invasive carcinomas with *ERBB2* amplification is roughly half that of DCIS lesions with microinvasion[8, 9], where *ERBB2* gains are most prevalent[10, 11]. Repeated attempts at molecular stratification of DCIS have been inconclusive[12, 13], leaving open the question of whether there are cell-autonomous processes that restrain *ERBB2*-amplified premalignancies within the duct.

Part of the challenge in identifying such modifiers lies in the regulatory complexity of ERBB2[14], which heterodimerizes with multiple ErbB family members (including EGFR) and signals from different compartments within the cell. Receptor activation starts at the plasma membrane[15, 16], persists in some form after internalization[17], and retrograde transport can continue to the inner nuclear membrane[18]. Further, ErbB signaling is normally tempered by waves of short- and long-term feedback[19]. When ErbB-induced pathways become aberrant and chronic, the immediate effect of these feedback mechanisms may change and give rise to trajectories that are heterogeneous rather than homeostatic[20, 21].

Tools are limited for examining i) longer-term adaptations to chronic ErbB signaling or ii) early escape from the DCIS-like state, but there is a longstanding observation linking the two in 3D culture. Synthetic activation of ErbBs in breast epithelia causes hyperproliferative, polarity-disrupted “multiacini” that bear resemblance to microscopic DCIS escapees (DEs)[22-25]. Interestingly, global ErbB stimulation causes the DE phenotype in only a fraction of clones in the culture[22]. A mechanism for the incomplete penetrance of DEs has evaded conventional molecular-biology[26] and transcriptomic[27] approaches. The phenotype is reportedly not heritable[22], but neither is it completely random, because DE frequency is dependent on the specific ErbB dimer[22, 23]. Genes that synergize with other oncoproteins in 3D culture do not with dimerized ErbBs[28], and those that independently drive DEs usually antagonize the ability of ErbB dimers to induce more[29, 30]. Candidates with synergy lack evidence of variable induction or activation when ErbBs are dimerized[31, 32], questioning their role as authentic effectors of ErbB-associated DEs. Here, we applied a frequency-matching approach to identify a critical ErbB-dependent karyopherin network that suggests a broader role for nucleocytoplasmic transport in the feedback regulation of chronic signaling and its emergent properties.

RESULTS

Activated B2B1 cells elicit a late-developing DE phenotype that is incompletely penetrant. We built upon prior work by engineering MCF10A-5E breast epithelial cells[33] with separate chimeric receptors containing the intracellular domain of either human EGFR[23] or rat Erbb2[22] (Fig. 1a). The extracellular NGFR domain of each chimera prevents signaling from endogenous ErbB ligands; FKBP and FRB domains heterodimerize the carboxy termini upon addition of the synthetic ligand AP21967 (AP)[34]. Cells with ectopic NGFR-EGFR-FRB and NGFR-Erbb2-FKBP were selected subclonally for expression at levels comparable to endogenous EGFR and ERBB2 in breast cancer lines (Extended Data Fig. 1a). The leading clone (B2B1) modulated ERK1/2 and STAT1 pathways and induced canonical ErbB target genes when treated with AP in 3D culture (Extended Data Fig. 1b–e). B2B1 cells thus provided a means to investigate ErbB responses initiated by a single, biologically relevant heterodimer pair[14].

Phenotypically, AP treatment uniformly increased outgrowth of B2B1 structures within 24 hours and sustained it for at least nine days (Extended Data Fig. 1f). However, consistent with published results[22, 24], we found that only ~35% of outgrowths exhibited a DE morphology of lost polarity and sphericity (Fig. 1b,c). Although DEs were obvious at 72 hours and detectable at 48 hours after AP addition, there was no clear indication before that despite persistent signaling from heterodimerized ErbBs for at least 24 hours (Fig. 1d, Extended Data Fig. 1b–d and Supplementary Video 1). Earlier studies of feedback did not look beyond 3–4 hours of ErbB stimulation[19, 35], leaving open the question of what adaptations were involved and how multi-cell fates could diverge so markedly.

Guilt-by-association candidates identified through stochastic frequency matching. New approaches are emerging to link phenotype variability with upstream heterogeneities in cell state[36, 37], but such methods are not yet ready to tackle multicellular phenomena like DEs. We adopted a premise similar to this recent work and its predecessors[38-40] by postulating that heterogeneous transcriptional states preceded and primed the emergence of DEs (Fig. 1e). To identify state heterogeneities among different outgrowths, we combined robust 10-cell transcriptomics obtained by laser-capture microdissection with the principle of stochastic profiling for cell-state inference[33, 41, 42]. Here, each 10-cell sample was collected from a separate outgrowth (Fig. 1e, boxes) and restricted to cells of the periphery, recognizing that DE-relevant changes occur in this subpopulation[24]. We collected samples from 20 outgrowths with or without AP heterodimerization along with 16 pool-and-split 10-cell equivalents for each condition that control for technical variability[33, 41, 43]. Across (20 + 16) x 2 = 72 samples, we quantified 10,373 ± 1118 gene targets (mean ± s.d.) at a detection $p < 0.1$ for analysis. Applying existing pipelines for distinguishing biological variability from technical noise[41], we predicted significant biological heterogeneity for 297 and 426 gene targets among B2B1 outgrowths ∓AP

respectively (Fig. 1f and Supplementary Tables 1 and 2). We hypothesized that one or more drivers of the DE phenotype resided within this set of targets.

To winnow targets further, we leveraged the known frequency of DEs anticipated in the days after stochastic profiling was performed (Fig. 1c). Envisioning future DEs as a binomial process with a 35% probability of "success", the goal was to identify gene-expression states with a probability similar or identical to DEs. Gene targets were prioritized by quantifying unexpectedly low or high expression states as successes and comparing this number to the likely range of DEs expected from 20 random draws. For each gene, we defined the threshold of success at the 10th and 90th percentiles for the minus-AP distribution of 10-cell samples (Fig. 1g, dashed lines). The threshold was motivated by the 10% background rate of DEs (Fig. 1c) attributable to the weak spontaneous dimerization of inactive ErbBs (K_D ~ 37 μM[44]). Using these thresholds, the number of successes was scored for the corresponding gene in the plus-AP condition and compared to the probability of observing such a number at a 35% probability of success (Fig. 1g,h). By requiring the stochastic frequencies of gene success and phenotype success to match, it created a stringent guilt-by-association filter for plausible upstream regulators of DEs. The approach identified 15 high-priority targets within the interquartile range and another 86 candidates within the 90% confidence interval of the expected value (0.35 x 20 = 7; Supplementary Table 3). The 426/15 = 28-fold reduction in high-priority targets enabled gene-by-gene perturbations that were consistent with broader pathways or biological categories enriched in the 426/(86+15) = 4-fold reduced set of candidates overall.

DE penetrance is perturbed by effectors of nucleocytoplasmic transport. High-expression states denoted success for nearly all genes that emerged from stochastic frequency matching (Fig. 1h, upper). We reasoned that it would be harder to increase DE frequency than to decrease it[45] and thus adopted an inducible-overexpression approach to screen targets. Genes were induced at the same time as AP addition to homogenize cells in the high state as ErbBs were activated. By comparing 3D cultures ±AP and ±induction with doxycycline (DOX), we could test for two-way statistical interactions (P_{int}) between the induced target and the penetrance of DEs caused by ErbB heterodimerization.

Within the 15 high-priority targets lay *XRCC6* and *TTI1*, raising the possibility that a heterogeneous DNA damage-like response was involved[46, 47]. Yet, induction of either gene had no detectable effect on AP-induced DEs compared to the minus-DOX condition or induced luciferase control (Extended Data Fig. 2a–c), prompting us to look more broadly. We combined all viable targets (15 + 86 – [4 uncharacterized loci and probeset redundancies] = 97 genes) and performed gene ontology (GO) enrichment analysis, identifying enriched GO Biological Processes related to localization and transport (Extended Data Fig. 2d). Among candidates, there were multiple genes connected to cytoskeletal trafficking: *KIF20A*, *DYNLL2*, *MTUS1*, and *PFN2*. However, inducing any of these genes did not promote more DEs but instead nearly abolished them (Extended Data Fig. 2e–h). The results

excluded a pervasive role for cytoskeletal trafficking and suggested that loss of DEs might generically indicate outgrowths that are unfit[45]. Consistent with this notion, we arbitrarily induced *BCAS2*, a candidate tied to pre-mRNA splicing[48] that resides within a breast-cancer amplicon[49], and found that it similarly blocked DEs (Extended Data Fig. 2i).

We arrived at a different conclusion for a set of genes tied to nucleocytoplasmic transport (Fig. 2a–d). The exportin *CSE1L* scored as a high-priority target for two probesets and synergistically increased the frequency of DEs when induced (Fig. 2a). This result was further complemented by loss-of-function studies in which inducible CSE1L knockdown significantly inhibited the AP stimulation of DEs (Fig. 2e and Extended Data Fig. 2j). Another high-priority target in this group was the nuclear pore-interacting protein *NPIPB11* (originally annotated as *LOC728888*), which significantly elevated AP-independent DEs in B2B1 cells (Fig. 2b). Further work on NPIPB11 was precluded by difficulties in achieving reliable protein overexpression, as reported elsewhere[50]. The nuclear pore subunit *NUP37* and the importin *KPNB1* were both candidates by stochastic frequency matching and antagonized the ability of ErbB heterodimerization to induce DEs (Fig. 2c,d). The NUP37 effect was much more potent, and loss-of function studies argued against a generic fitness defect upon perturbation, as inducible NUP37 knockdown significantly increased the frequency of basal DEs (Fig. 2f). Nevertheless, the direction of change for NUP37 perturbations was opposite that predicted by stochastic frequency matching, suggesting a role as an attenuator of DEs instead of a driver like CSE1L.

Stochastic frequency matching accurately nominated upstream DE regulators, but could they have been uncovered by more conventional approaches? We measured transcript abundances in bulk 3D cultures at 24 hours (when stochastic profiling was performed; Fig. 1e) or 72 hours (when DEs were evident; Fig. 1d) and found surprisingly few differences with or without AP (Fig. 1g–j). Most genes of interest were not detectably altered, and the leading DE driver (*CSE1L*) was not increased more than 1.4-fold above minus-AP control even after 72 hours of ErbB heterodimerization (Fig. 1g). Another karyopherin, the importin *KPNA2*, was more differentially abundant than *CSE1L* yet was not flagged as a cell-state heterogeneity (P_{het} = 0.26 vs. P_{het} = 0.0016 [probeset 1], 0.024 [probeset 2] for *CSE1L*) and did not perturb DE frequency when ectopically induced (Extended Data Fig. 2k,l). We concluded that our approach was effective at revealing hidden drivers of incomplete penetrance and turned our attention to the general significance of CSE1L for ErbB regulation.

Cse1l promotes macroscale DE-like organization of *Erbb2*-amplified allografts. To go beyond B2B1 cells and ErbB activation with synthetic ligands, we sought a very different cancer-relevant setting to test the role of nucleocytoplasmic transport. Transformed cells with constitutive ErbB signaling by mutation or amplification were of interest, but chronic ErbB activity would not capture the intermediate steps related to DEs. We mimicked this context by examining release from cytostatic doses of the dual ErbB inhibitor, lapatinib, in TM15 clone 6 (TM15c6) cells derived from an *Erbb2*-amplified tumor of a

P_{MMTV}-Cre;Erbb2$^{+/V660E}$ knockin mouse[51-53]. 3D cultures of TM15c6 cells were seeded in the presence of 2 μM lapatinib and grown for six days before lapatinib was washed out and outgrowth trajectories assessed. TM15c6 cultures did not exhibit DEs with all-or-none penetrance like those of nontransformed B2B1 cells, but lapatinib release caused significant decreases in circularity among the upper 35th percentile of outgrowths by size (Fig. 3a; percentile threshold selected to match DE penetrance in B2B1 cells). Circularity is a scaled area-to-perimeter ratio that does not depend on geometric size, and we saw little evidence of any confounding area-circularity relationship in TM15c6 cultures for up to five days after lapatinib release (Extended Data Fig. 3a). These data established a foundation for genetic perturbations of Cse1l in TM15c6 cells.

We began with inducible ectopic expression of human CSE1L in TM15c6 cells (Extended Data Fig. 3b), using the same experimental paradigm as in B2B1 cells but substituting lapatinib release for AP addition. Relative to the pre-release circularity of each genotype, there was an exaggerated reduction in circularity when CSE1L was co-induced with the washout of lapatinib (Fig. 3b). The CSE1L result was not heavily dependent on the upper percentile of outgrowths considered (Extended Data Fig. 3c). Reciprocally, inducible knockdown of Cse1l severely attenuated the loss of circularity from lapatinib release, and this phenotype was reverted upon co-induction of human CSE1L as an RNAi-resistant addback (Fig. 3c,d and Extended Data Fig. 3d). Therefore, acute reactivation of ErbB signaling in TM15c6 mammary carcinoma cells elicits a Cse1l-dependent multi-cell phenotype that is very reminiscent of DEs.

DCIS escape in vivo entails many additional barriers that are not reflected in 3D culture[54, 55]. As a surrogate, we administered luciferase-expressing TM15c6 cells into the 4th and 9th mammary ducts of SCID-beige mice in a paired design that compared inducible shCse1l to contralateral control[56, 57]. shRNAs were pre-induced in cells before administration, and animals were fed DOX-containing food for one week before surgery and thereafter[58]. Despite prior Cse1l depletion, bioluminescence was comparable between genotypes within the cohort at two days post-inoculation (P = 0.44; Extended Data Fig. 3e), indicating that Cse1l knockdown does not discernibly influence intraductal colonization. For the subsequent six days, we administered lapatinib daily at a low dose (30 mg/kg) that forestalled lesion growth as quantified midway by bioluminescence (P = 0.93 [control], 0.14 [shCse1l] compared to Day 2; Extended Data Fig. 3e). Then, lapatinib was stopped and animals were imaged twice weekly until tumor bioluminescence was comparable between shCse1l and control glands at 22 days (P = 0.48; Extended Data Fig. 3e). Although both genotypes had invaded the stroma by this time, we posited that the tortuosity of the final tumors would reflect DE propensity of TM15c6 cells at earlier stages. When glands were excised and tumors imaged ex vivo for higher resolution assessment of macroscale organization, we found that shCse1l tumors were consistently more circular than paired controls (Fig. 3e). Across the cohort, tumor circularity did not relate significantly to tumor mass (Extended Data Fig. 3f), excluding differences in net growth as a confounder. The TM15c6 study—with

its change in species (human to mouse), ErbB activator (AP to lapatinib release), and cellular context (in vitro to in vivo)—strengthens the general conclusion that CSE1L/Cse1l drives DE-like phenotypes at the onset of persistent ErbB signaling.

CSE1L-associated network states inhibit import of classical nuclear localization signals. The results with CSE1L, NUP37, NPIPB11, and KPNB1 in B2B1 cells (Fig. 2) justified examining other known regulators of nucleocytoplasmic transport. The pleiotropic exportin *XPO1* was detected as a biologically variable transcript by stochastic profiling in AP-treated cells but at a reduced expression frequency and with bulk changes that were muted compared to *CSE1L* (Extended Data Fig. 4a and Supplementary Table 3). Transport to and from the nucleus depends critically on nucleocytoplasmic gradients of the Ran GTPase[59]—although not measurably heterogeneous, *RAN* and its binding partners (*RANBP1* and *RANBP3*) were retained or elevated upon prolonged ErbB heterodimerization (Extended Data Fig. 4b–d). Conversely, factors regulating RanGTP hydrolysis (*RANGAP1*) and RanGDP exchange (*RCC1* and *NUTF2*) were not significantly altered, but independent bulk replicates of B2B1 cultures exhibited surprising dispersion (Extended Data Fig. 4e–g). We clustered the bulk transcript profiles by replicate and noted covariations among *KPNA2*–*KPNB1*, *CSE1L*–*XPO1*, and *RANBP1* that were nominally offsetting and thus difficult to interpret (Extended Data Fig. 4h). These observations suggested a need to examine nucleocytoplasmic transport at the systems level.

Drawing from earlier efforts[60, 61], we built a multicompartment systems model encoding nuclear import and export with the Ran transport cycle (Fig. 4a and Supplementary Note 1). For consistency, the model retains common-name designations from before[60, 61]: CAS for CSE1L, Imp-α as a lumped parameter for KPNA1 through KPNA7, Imp-β for KPNB1, NTF2 for NUTF2, and CRM1 for XPO1. Changes in model parameters were not permitted unless a typographical error was discovered or the original parameter could not be definitively identified (Supplementary Note 1). To consider rate-limiting roles for NUP37 or NPIPB11, the model was elaborated with two classes of nuclear pores, one of which was selective to proteins harboring specific classes of nuclear localization sequences. However, this change proved inconsequential given the estimated number of nuclear pores per cell (Supplementary Note 1). The abundance of all protein species in the model was calibrated to B2B1 cells by quantitative immunoblotting against HeLa cells used in the prior work[60, 61] to arrive at a draft model for validation (Supplementary Note 1 and Supplementary Table 4).

We tested the fidelity of the calibrated model by designing a series of inducible “tandem cargo reporters” harboring fluorescence proteins, epitope tags, and recognized sequences for import and export (Extended Data Fig. 4i). Reporters were individually induced at a few million copies per B2B1 cell and triply localized by immunostaining to mitigate the effect of cleavage products; then, images were aggregated and segmented for estimating nuclear-to-cytoplasmic (N/C) ratios at steady state in single cells (Extended Data Fig. 4i–k). All reporters contained an offsetting nuclear export sequence

(NES) to distinguish the potency of each class of nuclear localization sequence (NLS)—a monopartite NLS from simian virus 40 T antigen ($NLS_{SV40Tag}$), a bipartite NLS from Cbp80 ($2xNLS_{Cbp80}$), or the Imp-β-binding domain of KPNA2 (IBB_{KPNA2}). $NLS_{SV40Tag}$ and $2xNLS_{Cbp80}$ are recognized by Imp-α:Imp-β dimers with different affinity ($K_{D,SV40Tag}$ ~ 32 nM[62], $K_{D,Cbp80}$ ~ 2.5 nM[63]), whereas IBB_{KPNA2} is imported after binding Imp-β alone[61] ($K_{D,IBB}$ ~ 6.5 nM[62]). We found that the tandem cargo reporters yielded different predictions of N/C ratio in the model, and these predictions compared very favorably to measured values averaged across the population (Fig. 4b–d and Extended Data Fig. 4l). Because no recalibration was needed for any tandem cargo reporter, the experimental tests validated the model for provisional use.

Next, we predicted changes in steady-state N/C ratio for the different cargo classes when species abundances (initial conditions) of the model were perturbed combinatorially. Biologically realistic combinations were gleaned from the transcriptomic data collected among single B2B1 outgrowths during stochastic profiling (Fig. 4e). We found that presence of an NES had very little impact on the change of any reporter, consistent with its somewhat weaker potency[64] and the limiting abundance of the CRM1 cofactor RanBP3[65] in B2B1 cells (Supplementary Note 1). The outgrowth-to-outgrowth patterns of $NLS_{SV40Tag}$ and $2xNLS_{Cbp80}$ were also quite similar, owing to their same connectivity in the model (Fig. 4a,e). A cluster of perturbations with high N/C ratio for these reporters was notable (Fig. 4e, dashed), and thus we stratified at the upper 35th percentile to ask whether any initial conditions were significantly associated. The analysis identified a significant positive association with Imp-α, but not Imp-β, and a negative association with CAS/CSE1L (Fig. 4f–h). By contrast, IBB_{KPNA2} engaged the network differently[61] and showed its own sensitivity to combinatorial perturbations, including a positive association for Imp-β and a negative association with CRM1/XPO1 (Extended Data Fig. 4m,n). The modeling results suggested a natural antagonism between karyopherins that depended on the type of cargo transported.

CSE1L–NUP37 proximity interactomes contain ErbBs. It was centrally important to identify cargo that could be directly relevant to the DE phenotype. Because transport interactions are very transient, we developed a proximity-labeling[66] approach focused on CSE1L and NUP37—two confirmed effectors that strongly perturb DE penetrance (Fig. 2a,c). Although *CSE1L* and *NUP37* transcripts are coexpressed broadly[67], there are no reports of binary or tertiary interactions involving these proteins. Thus, novel proximity interactions shared by CSE1L and NUP37 should strongly suggest conduits for the DE phenotype.

We scaled up from 3D culture to 15-cm plates by growing B2B1 cells as domes overlaid with dilute matrigel, a format that mimics 3D transcriptional changes for up to 10 days[68]. Lines expressing CSE1L or NUP37 fused to a promiscuous biotin ligase (BirA*) were moderately induced for 24 hours (Extended Data Fig. 5a,b), followed by heterodimerization for 24 hours and biotin labeling for 24 hours

after that (Fig. 5a). Due to the overlay format, solubilized extracts contained many adsorptive extracellular matrix components[69] that required a more-stringent two-step purification of biotinylated target proteins (Fig. 5a). Sequential selection with anti-biotin and streptavidin yielded many proximity interactions detectable by mass spectrometry (MS) after SDS-PAGE purification of eluted products (Fig. 5b,c and Supplementary Table 5). The MS data contained multiple known interactors for CSE1L and NUP37 previously identified by co-immunoprecipitation, crosslinking, or yeast two-hybrid (Fig. 5c). We specifically confirmed literature-derived interactions by immunoblotting anti-biotin immunoprecipitates from independent samples: KPNA2, RAN, and p53 for CSE1L (Fig. 5d,e) and Sec13, NUP160, and KPNA2 for NUP37 (Fig. 5f,g). Proteins sequestered from CSE1L or NUP37 were not detectably biotinylated, verifying the approach.

For uncovering novel proximity interactions in the MS data, we used a contaminant repository[70] to identify proteins that rarely appear in BirA* datasets (Fig. 5c and Supplementary Table 5). Among the dozens of proteins that passed the criterion, roughly half overlapped between the CSE1L and NUP37 datasets ($P < 10^{-13}$ by hypergeometric test). Strikingly, both studies identified EGFR, ERBB2/Erbb2, and the EGFR endocytic-trafficking adaptor SH3KBP1[71] as stringent proximity interactions (Fig. 5c and Supplementary Table 5). We independently verified the MS result by immunoblots for the EGFR and Erbb2 chimeras, quantifying extents of proximity labeling in the range of known interactions (Fig. 5d–g). CSE1L was previously reported in MS data from EGFR immunoprecipitates[72]; we confirmed this interaction but found that Erbb2 was labeled much more efficiently than EGFR (Fig. 5d,e). The same was not true in B2B1 cells expressing BirA*-NUP37, where EGFR and Erbb2 were labeled equally well (Fig. 5f,g). This ruled out differences in chimera abundance as an explanation for the Erbb2-biased CSE1L result. CSE1L strongly increases DE penetrance (Fig. 2a), and EGFR homodimers lacking Erbb2 do not elicit a DE phenotype[22]. The data suggested that nucleocytoplasmic transport of Erbb2-containing dimers themselves might dictate penetrance of the phenotype they evoke.

DE penetrance is inhibited by EGFR–Erbb2 trafficking from the plasma membrane. Proximity labeling of EGFR or Erbb2 was not detectably altered by heterodimerization with AP (Fig. 5d–g), raising the question of what cell biology was initiated by the stimulus (Fig. 1c). Upon ligand activation at the plasma membrane, ErbBs are internalized within a few minutes[73] and can traffic to the nucleus in less than a half an hour[74]. We cultured B2B1 cells on coverslips and observed transient nuclear accumulation of colocalized EGFR–Erbb2 after 15 and 30 minutes of heterodimerization, which subsided at one hour and disappeared at four hours as the receptor was downregulated (Fig. 5h). Interestingly, after recovery in the presence of AP for 24 hours, we quantified sustained EGFR–Erbb2 immunoreactivity in the nucleus that was nearly as intense as at early times after stimulation. This long-term nuclear localization coincided with the DE decision point (Fig. 1d,e), raising the possibility it

could be relevant to phenotype penetrance. We tested the impact of ErbB internalization by mildly reducing clathrin heavy chain (CLTC) in B2B1 cells to impair clathrin-mediated endocytosis[75] (Extended Data Fig. 5c). CLTC knockdown did not alter abundance of the ErbB chimeras, but CLTC-deficient cells exhibited significant increases in the frequency of DEs (Fig. 5i and Extended Data Fig. 5d), indicating that internalized EGFR–Erbb2 complexes are repressive.

EGFR and Erbb2 chimeras are recognized by Imp-α:Imp-β as classical cargo. ErbB recruitment to the nucleus occurs when a polybasic juxtamembrane segment within the ErbB sequence acts as a tripartite NLS for transport[74, 76]. We returned to the systems model of nucleocytoplasmic transport (Fig. 4a) and asked how steady-state transport of different cargoes depended on the abundance of proteins in the network (Fig. 6a–e and Extended Data Fig. 6a–f). For the B2B1 model, NES-harboring cargoes were distinguished only when RanBP3 abundances were very high (Fig. 6a), allowing us to ignore consideration of ErbB–CRM1 interactions[77, 78] in this setting. Further simplifying the analysis, we found that the sensitivities of monopartite ($NLS_{SV40Tag}$) and bipartite ($2xNLS_{Cbp80}$) NLS cargoes were identical except for an offset in N/C ratios from differences in affinity for Imp-α:Imp-β (Supplementary Table 4). By contrast, IBB_{KPNA2} cargo was more sensitive to CAS/CSE1L and Ran abundance, and transport qualitatively differed in response to the abundance of Imp-α and Imp-β (Fig. 6b–e). ErbBs bind Imp-β[78] but evidence for or against interactions with Imp-α was lacking. Systems-level analysis of ErbB nucleocytoplasmic transport thus required clarification of whether EGFR–Erbb2 heterodimers acted as classical NLS-like cargo or instead as non-classical IBB-like cargo[79].

To verify EGFR–Erbb2 interactions with Imp-β and test for interactions with Imp-α, we probed for epitope-tagged karyopherins in EGFR and EGFR–Erbb2 immunoprecipitates. B2B1 cells modestly expressing inducible KPNA2 (115 ± 10% of endogenous) or KPNB1 (80 ± 9% of endogenous) were probed for epitope tag after immunoprecipitation of the EGFR chimera with or without prior AP treatment. We observed robust increases in co-immunoprecipitating Erbb2 chimera upon heterodimerization, as expected, and both KPNA2 and KPNB1 were consistently detectable in all immunoprecipitates (Fig. 6f,g). After scaling for target enrichment, there was no discernible difference in the level of KPNA2 vs. KPNB1 co-immunoprecipitation (Fig. 6g), suggesting the two karyopherins bind with roughly equal stoichiometry.

As a complementary approach, we evaluated potential interactions by proximity ligation assay[80] (PLA). We confirmed assay specificity with positive and negative controls, as well as heterodimerizer-regulated proximity of EGFR and Erbb2 chimeras (Fig. 6h and Extended Data Fig. 6g,h). Above-background proximity ligation was observed for all ErbB-karyopherin pairs, with some signals approaching the saturated spot detection of the KPNA2:KPNB1 positive control (Fig. 6i,j). PLA spots often increased after extended heterodimerization, probably reflecting the increased stabilization of ErbB chimeras (e.g., Fig. 5d) more so than an increase in karyopherin binding. Together, we conclude

that ErbBs bind the nuclear-transport machinery through an Imp-α:Imp-β heterodimer like classical NLS cargo.

Nuclear EGFR–Erbb2 engages a miR-205–KPNA1 negative-feedback circuit. Retrograde ErbB transport to the nucleus has been delineated mechanistically, but its consequences are multifaceted and contextual[18]. Nuclear ErbBs are reported to act as transcriptional coactivators[81, 82] and chromatin-binding factors[74, 82, 83]. Therefore, we asked whether specific genomic loci were bound constitutively or inducibly to EGFR–Erbb2. By confocal imaging of 3D cryosections, we found EGFR–Erbb2 colocalized in the nucleus, and nuclear immunoreactivity increased significantly with the addition of AP for 24 hours (Fig. 7a and Extended Data Fig. 7a). To preserve this 3D context as best as possible, input chromatin was prepared from B2B1 cells cultured in the overlay format for one week ± AP added on the sixth day. ErbB chimeras were immunoprecipitated by their respective C-terminal epitope tags and processed for chromatin immunoprecipitation sequencing (ChIP-seq) to identify enriched loci above naive IgG controls. For two different anti-epitope antibodies against the Erbb2 chimera, we immunoprecipitated comparatively little chromatin and were unable to detect any reliable enrichment peaks. This result is consistent with previous work involving ERBB2-amplified cells[82] and suggests that the C terminus is mostly obscured in the nucleus after fixation. ChIP-seq of B2B1 samples was successful when immunoprecipitating EGFR chimeras, and we recurrently identified enriched binding peaks for 26 loci without AP and 51 loci with AP, 17 of which were common to both conditions (Fig. 7b and Supplementary Table 6).

As reported[84, 85], EGFR occupancy often occurred along the gene body of highly expressed genes (*TXNIP*, *NEAT1*) and transcription factors of the AP1 (*JUNB*) and KLF (*KLF5*) families. The AP-independent loci contained multiple genes previously linked to 3D cell-to-cell heterogeneity in MCF10A-5E cells: *KRT5*, *NFKBIA*, and *SOD2*[33, 58, 68]. These transcripts showed various time- and AP-dependent patterns of change, but none had been nominated as DE candidates by the earlier frequency-matching approach (Extended Data Fig. 7b–d and Supplementary Table 3). Instead, our attention turned to the *MIR205HG* locus encoding miR-205 (Fig. 7b), an epithelial microRNA frequently misregulated in cancer[86]. Although the earlier transcriptomic data could not be used to analyze miRNA abundance, miR-205 is known to be reduced by chronic ERBB2 signaling through changes in DNA methylation[87, 88]. We confirmed miR-205 downregulation in B2B1 cells after three days of AP treatment but noted that the change was time dependent, reversing and becoming more variable when measured two days earlier (Extended Data Fig. 7e). Further, miR-205 abundance significantly increased when B2B1 cells were acutely heterodimerized in overlay cultures that improve uniformity of the response (Fig. 7c). As with other loci, EGFR occupancy covered the *MIR205HG* promoter and length of the gene body (Fig. 7d). We used ChIP-qPCR to confirm specificity and AP-independence of binding (Fig. 7e); presumably, effects on the *MIR205HG* locus change when bound EGFR is co-associated with active

Erbb2 (Fig. 7c). Analogously, EGFR–Erbb2 heterodimers strongly elicit a DE phenotype, whereas EGFR homodimers do not[22, 23].

miR-205 posttranscriptionally regulates many genes[86], but one compelling target is the Imp-α family member *KPNA1*[89]. The 3' UTR of human *KPNA1* contains three predicted[90] binding sites for miR-205, the most proximal of which is broadly conserved, and we confirmed that miR-205 suppresses endogenous KPNA1 (Fig. 7f and Extended Data Fig. 7f)[89]. By immunofluorescence, KPNA1 protein expression was highly mosaic among single cells in B2B1 outgrowths (Fig. 7g). Importantly, KPNA1 protein abundance declined significantly upon addition of AP heterodimerizer without detectable changes in *KPNA1* mRNA, implicating a posttranscriptional mechanism (Fig. 7h and Extended Data Fig. 7g). When B2B1 cells were engineered with inducible ectopic KPNA1 lacking the native 3' UTR targeted by miR-205, we found that heterodimerizer-induced DEs were almost completely abolished (Fig. 7i). This result starkly contrasted earlier results with KPNA2 that showed no effect upon ectopic expression (Extended Data Fig. 2i). Imp-α isoform switching has been linked to cell fate determination in other settings[91], and the miR-205–KPNA1 circuit induced by nuclear ErbBs added an isoform-specific negative feedback to the regulation of DEs.

Nucleocytoplasmic regulation of ErbBs gives rise to species-specific ultrasensitivity. The earlier systems model of nucleocytoplasmic transport predicted opposite effects of Imp-α and CAS/CSE1L abundance on the steady-state accumulation of classical cargo. Elevating Imp-α (e.g., KPNA1) increased N/C ratio of cargo and decreased DE penetrance (Fig. 4f and 7i), whereas high CAS/CSE1L decreased N/C ratio and increased DE penetrance (Fig. 2a and 4h). We thus modeled internalized ErbB heterodimers as classical cargo with an unknown affinity for Imp-α:Imp-β, equating high C/N [= $(N/C)^{-1}$] ratio at steady state with the DE phenotype (Fig. 7j). Imp-α and CAS/CSE1L abundances reciprocally affected C/N ratio across a wide range of binding strengths (Fig. 7j). However, model predictions were more sensitive to Imp-α than CSE1L except for very high abundances, and the changes in C/N ratio were too gradual to explain how two DE states could coexist in the same population of cells.

We next considered the antagonistic feedbacks elaborated before. Active ErbBs internalize and traffic toward the nucleus, but they also induce *CSE1L*, which is predicted to inhibit ErbB nuclear transport by competing for available Imp-α (Fig. 2g, 4a, and 5h). In parallel, nuclear ErbB heterodimers repress KPNA1 through miR-205, reducing nuclear transport and exacerbating the CSE1L competition with the Imp-α that remains (Fig. 7f–i and Extended Data Fig. 7f). After combining transcriptional, posttranscriptional, and cell-biological circuits, the overall ErbB feedback architecture (Fig. 7k, upper) is reminiscent of a synthetic-biology toggle switch capable of mixed single-cell behavior[92].

To determine whether cells were operating close to a mixed regime, we added proportional feedbacks from cytoplasmic ErbBs to CAS/CSE1L (positive) and from nuclear ErbBs to Imp-α

(negative; Fig. 7k, upper). Repeating the simulations with the revised feedback architecture completely changed the dependence of C/N ratio on Imp-α and CAS/CSE1L. Sensitivity to overall Imp-α levels was severely blunted, consistent with results for KPNA2 (Extended Data Fig. 2i), and the response to CSE1L became switchlike over a narrow range of expression (Fig. 7k, lower). We further noted that CSE1L abundance heterogenizes upon ErbB activation, with a range of expression that more than doubled after 24 hours of AP addition (Extended Data Fig. 7h). The revised model indicates that very small initial differences in CSE1L are sufficient to yield divergent outcomes due to the nucleocytoplasmic transport properties of ErbB.

A key prediction of the ErbB transport model is that switch-like ultrasensitivity to CSE1L will decline when ErbB cargo affinity for Imp-α:Imp-β is reduced (Fig. 7k, right). In this scenario, the low-C/N, low-DE state is less dramatic, and prevalence of the DE phenotype should increase. We compared the tripartite NLSs from several extant species and found one R679Q variation, which was primate specific and predicted[93] to have weaker NLS potency (Fig. 7l). As tandem cargo reporters, the tripartite sequences of human EGFR and human ERBB2 were active but considerably weaker than that of rat Erbb2 (Extended Data Fig. 7i–k). To test the model prediction, we established independent EGFR-expressing clones wherein chimeric receptors of rat Erbb2 and human ERBB2 were comparably abundant (Extended Data Fig. 7l). For both rat-human pairs, DE penetrance was significantly increased for the human clone relative to the rat clone (Fig. 7m). These results reinforce the model-driven assertion that DE and non-DE fates co-occur in ErbB-activated breast and mammary epithelia because of feedback regulation of active receptors and their transport to the nucleus.

DISCUSSION

This study unravels a set of time-evolving, competitive feedbacks that unfold hours to days after activation of ErbB2/HER2. CSE1L is a hallmark target gene of E2F[94], which becomes activated indirectly by cyclin D1 induction from immediate-early AP1-family transcription factors that are induced and stabilized by sustained ERK signaling from receptor tyrosine kinases[95, 96]. ErbB → CSE1L is slow because of the two rounds of signaling–transcription–translation required. Concurrently, active ErbBs are internalized and trafficked subcellularly, most toward endolysosomal degradation or recycling but some to alternative fates[74, 97] including the nucleus. Various roles have been ascribed to nuclear ErbBs[18]. Our results are most concordant with work reporting ErbB-RNA polymerase II co-occupancy along the body of actively transcribed genes[85] such as *MIR205HG*. Here, ErbBs may directly impact the tyrosyl phosphorylation of RNA polymerase II and its subsequent transcriptional activity[98, 99]. miR-205 transcription, maturation, and translational repression is slow and transient, yet human KPNA1 appears to be a particularly potent target impacting how internalized ErbBs are routed. An ErbB –| Imp-α relationship thus arises as a daisy chain of subcellular transport, signaling–transcription, and posttranscriptional regulation. Together, these feedbacks create a network architecture whose outcome is ultrasensitive to the initial abundance of CSE1L.

There are scattered reports of associations between HER2 signaling, nucleocytoplasmic transport, and CSE1L abundance in cancer. *ERBB2* and *CSE1L* amplifications are both frequent in medulloblastoma[100], and multiple HER2-positive breast cancer lines harbor separate gains in *CSE1L*[101]. As an exportin, CSE1L contains chemically reactive cysteines that are susceptible to covalent inhibition[102]. CSE1L inhibitors might one day serve as adjuvants for HER2-amplified cancers, just as a first-in-class covalent inhibitor of the exportin XPO1 now enhances standard of care for multiple myeloma[103]. Besides CSE1L upregulation, other cancers may subvert the acute effects of nuclear ERBB2 directly by mutation. The tripartite NLS of ERBB2 resides in the juxtamembrane segment, where recurrent NLS-damaging mutations have been documented in Arg678, Arg677, Arg683, and Arg688 (Fig. 7I); importantly, an R678Q mutation observed in gastric cancer promotes DE-like growth of MCF10A cells[104]. From this standpoint, the primate-specific R679Q variant of ERBB2 may be an important consideration in reconciling debates surrounding the (patho)physiological importance of nuclear ErbBs[105, 106].

We connected ErbB signaling to nucleocytoplasmic regulators by using a frequency-matching approach that statistically links transcript variability to phenotype variability. This guilt-by-association concept is effective when background fluctuations are mostly stochastic[107]. Measuring 10-cell transcriptomes from single outgrowths enabled us to retain DE-relevant fluctuations while averaging out single-cell confounders such as cell-cycle status[43, 108]. The method should be generally tractable for studying the molecular basis of incompletely penetrant phenotypes that are common and stereotyped,

irrespective of the time scale on which they operate. There are several regulatory topologies conferring ultrasensitivity that remain to be discovered in biological systems[109].

FIGURES

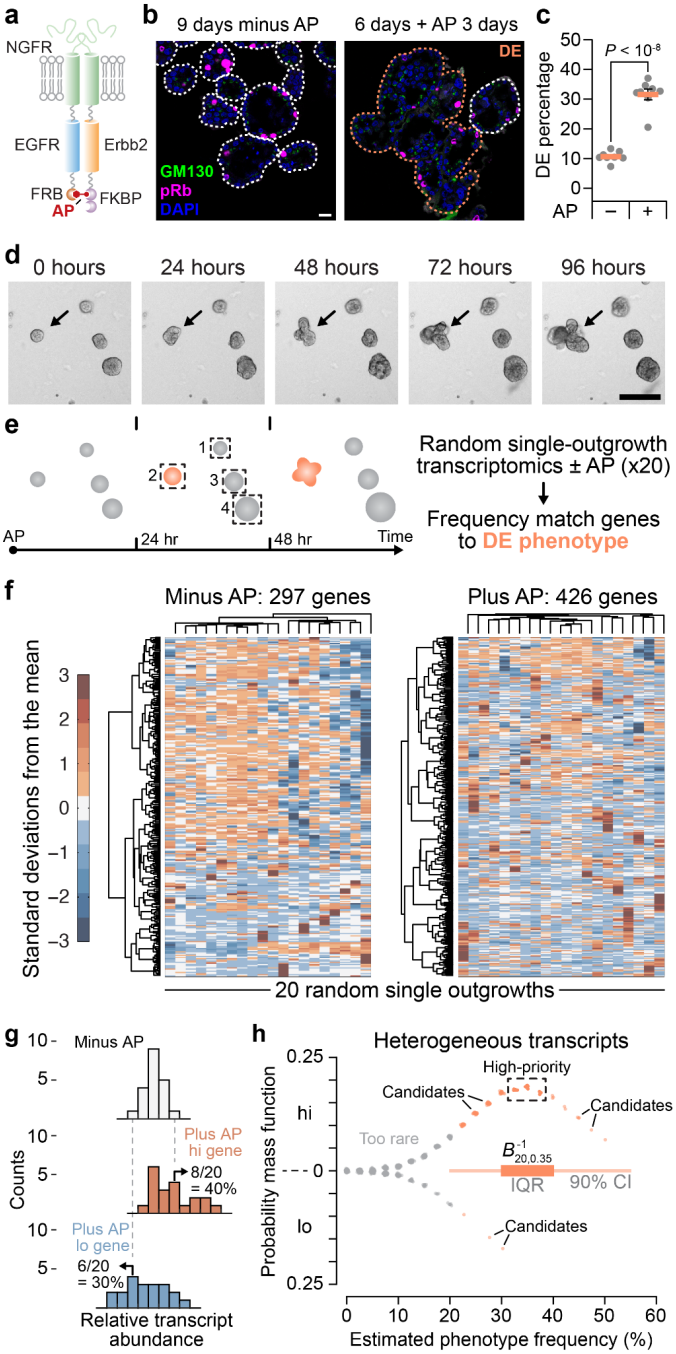

Fig. 1 | Candidate regulators of a fractionally penetrant outgrowth phenotype identified by stochastic frequency matching.

a, Molecular design of NGFR-EGFR-FRB[23] and NGFR-Erbb2–FKBP[22] chimeras heterodimerized by AP21967 (AP). MCF10A-5E cells[33] were serially transduced and subcloned to generate B2B1 cells.

b, ErbB heterodimerization causes a nonspherical DCIS escapee (DE) phenotype in 3D culture. B2B1 cells were cultured for 9 days with or without 0.5 μM AP for the final three days, stained for Golgi polarity (GM130, green) and proliferation (phospho-Rb [pRb], magenta), counterstained for nuclei (DAPI, blue) and membrane-ECM (wheat germ agglutinin [WGA], white), and imaged by confocal microscopy. One DE in the plus-AP condition is outlined, and the scale bar is 20 μm.

c, Fractional penetrance of the ErbB-induced DE phenotype in B2B1 cells. B2B1 cells were cultured in 3D for nine days with or without 0.5 μM AP for the final three days. Data are shown as the arcsine

transformed mean ± s.e. from n = 8 biological replicates where >200 outgrowths were scored per replicate. Differences were assessed by a two-sided t test after arcsine transformation.

d, DEs (arrow) are not apparent until after 48 hours of ErbB heterodimerization. B2B1 cells were 3D cultured for six days, treated with 0.5 μM AP for the indicated times, and serially imaged by brightfield microscopy. The scale bar is 200 μm.

e, Approach for stochastic frequency matching. After 24 hours of ErbB heterodimerization and before the appearance of DEs, 3D outgrowths (n = 20) were randomly sampled by laser-capture microdissection and assessed for transcriptional regulatory heterogeneities by stochastic profiling[33, 41]. Measured transcript fluctuations were then compared to the DE frequency estimated in **c**.

f, Outgrowth-to-outgrowth transcript heterogeneities identified by stochastic profiling of B2B1 3D cultures with or without 0.5 μM AP for 24 hours. Microarray probeset intensities were hierarchically clustered with Ward's linkage after row standardization.

g, Approach for quantifying transcript fluctuations. For each gene, the minus-AP condition (top) was used to specify 10th and 90th percentiles as gates to score the number of outgrowths above (middle) and below (bottom) the minus-AP control distribution for each gene.

h, Stochastic frequency matching gleans 86 candidate and 15 high-priority probesets from 426 outgrowth-to-outgrowth heterogeneities associated with ErbB heterodimerization. Probesets are jittered about the probability mass function for a binomial distribution (20 trials, 35% success probability) versus their estimated up or down expression frequency as in **g**. Probesets within the interquartile range (IQR) of the inverse binomial distribution ($B^{-1}_{20,0.35}$) were scored as high-priority, whereas those within the 90% confidence interval (CI) were considered candidates.

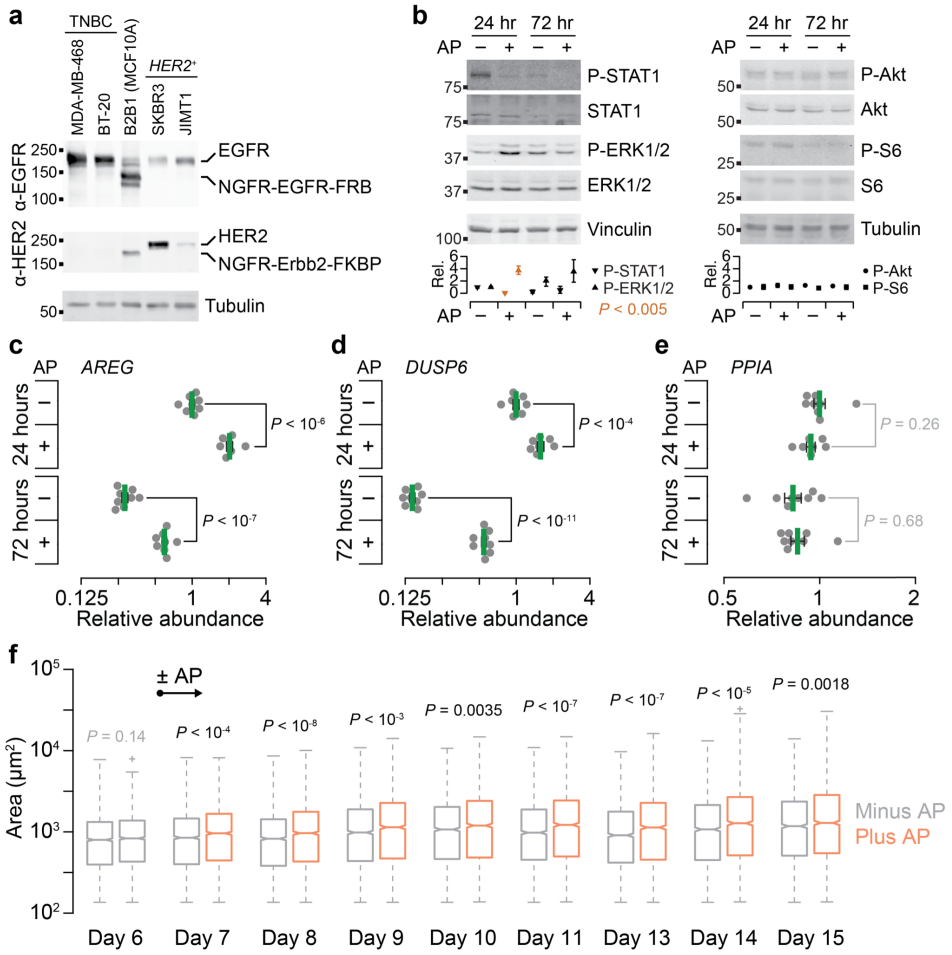

Extended Data Fig. 1 | A B2B1 subclone of MCF10A-5E cells with moderate ectopic expression of chemically activatable EGFR and Erbb2 chimeras.

a, Abundance of NGFR-EGFR-FRB and NGFR-Erbb2-FKBP chimeras in B2B1 cells is comparable to endogenous expression in triple-negative breast cancer (TNBC) and *HER2*-amplified (*HER2*$^+$) breast cancer lines respectively. Protein extracts were immunoblotted for EGFR and HER2 intracellular domains with tubulin used as a loading control.

b, ErbB heterodimerization alters phosphorylation of STAT1 (Tyr701) and ERK1/2 (Thr202/Tyr204) but not phosphorylation of Akt (Ser473) or S6 (Ser240/244). Protein extracts from 3D-cultured B2B1 cells treated with or without 0.5 μM AP for the indicated times after Day 6 were immunoblotted for the indicated proteins with total STAT1, total ERK1/2, total Akt, total S6, vinculin, and tubulin used as loading controls. Bottom graphs show replicated densitometry from n = 3 biological replicates; at each time point, differences between ±AP conditions were assessed by two-sided t test.

c–e, ErbB heterodimerization induces canonical ErbB target genes with no detectable effect on housekeeping genes. Quantitative PCR for *AREG* (**c**), *DUSP6* (**d**), and *PPIA* (**e**) in B2B1 cells cultured in 3D for six days followed by addition of 0.5 μM AP21967 (AP) for 24 hours or 72 hours where indicated. Data are shown as the geometric mean (normalized to the 24-hour, minus-AP condition) ± log-transformed s.e. from n = 7–8 biological replicates. Differences in geometric means were assessed by two-sided t test after log transformation.

f, ErbB heterodimerization causes a global and sustained increase in outgrowth size within 24 hours of AP addition. B2B1 cells were cultured in 3D for six days followed by stimulation with or without 0.5 μM AP for the indicated times after Day 6. Cross-sectional areas were quantified for n = 1851–2229 (Minus AP) or 1774–2317 (Plus AP) outgrowths from four biological replicates. Boxplots show the median area, estimated 95% confidence interval of the median (notches), interquartile range (box), 1.5x the

interquartile range from the box edge (whiskers), and outliers (+). Differences between groups for each time point were assessed by two-sided rank sum test with Šidák correction for multiple-hypothesis testing.

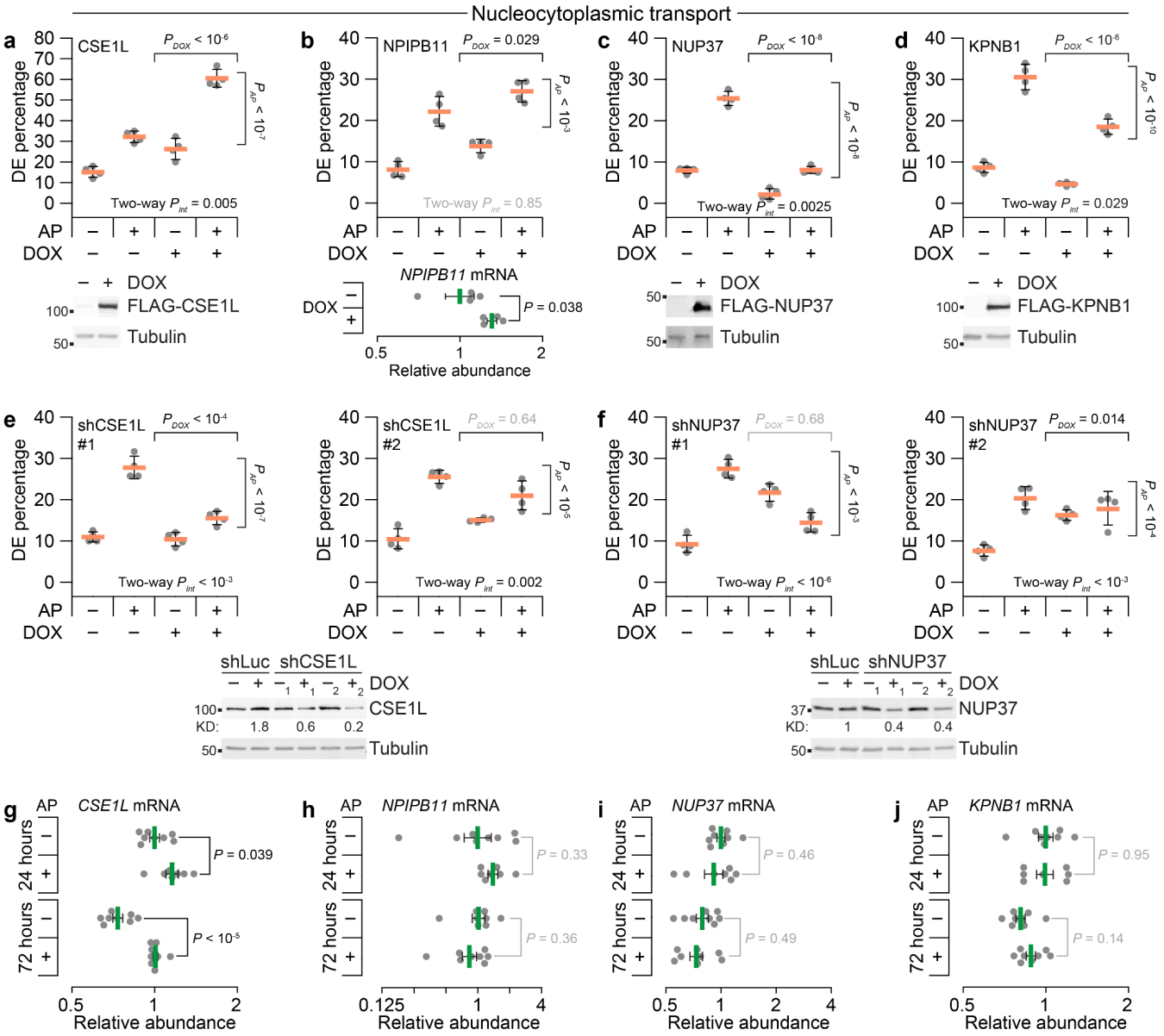

Fig. 2 | Acute gain- and loss-of-function approaches support a role for fractionally induced effectors of nucleocytoplasmic transport imperceptible at the population level.

a–d, Candidates related to nucleocytoplasmic transport affect DE penetrance induced by ErbB heterodimerization when ectopically expressed. B2B1 cells expressing inducible FLAG-tagged CSE1L (**a**), NPIPB11 (**b**), NUP37 (**c**), or KPNB1 (**d**) were used where indicated.

e, f, Loss of ErbB heterodimer-induced DEs upon inducible knockdown of nucleocytoplasmic regulators. B2B1 cells expressing inducible shCSE1L (**e**) or shNUP37 (**f**) were used where indicated.

g–j, Quantitative PCR for *CSE1L* (**g**), *NPIPB11* (**h**), *NUP37* (**i**), and *KPNB1* (**j**) in B2B1 cells cultured in 3D for six days followed by addition of 0.5 μM AP21967 (AP) for 24 hours or 72 hours where indicated. Data are shown as the geometric mean (normalized to the 24-hour, minus-AP condition) ± log-transformed s.e. from n = 7–8 biological replicates. Differences in geometric means were assessed by two-sided t test after log transformation.

For **a–f,** B2B1 cells stably expressing doxycycline (DOX)-inducible ectopic constructs were 3D cultured for 9–13 days with or without 0.5 μM AP added at Day 6 and/or 1 μg/ml DOX added at Day 5 where indicated. Data are shown as the arcsine transformed mean ± s.e. from n = 4 biological replicates where >100 outgrowths were scored per replicate. Differences by factor (DOX or AP) and two-factor interaction (int) were assessed by two-way ANOVA after arcsine transformation. Ectopic expression was confirmed

by immunoblotting for FLAG with tubulin used as a loading control, except for *NPIPB11* where induction was confirmed by quantitative PCR. Inducible knockdown was quantified relative to the no DOX shRNA control targeting luciferase (shLuc).

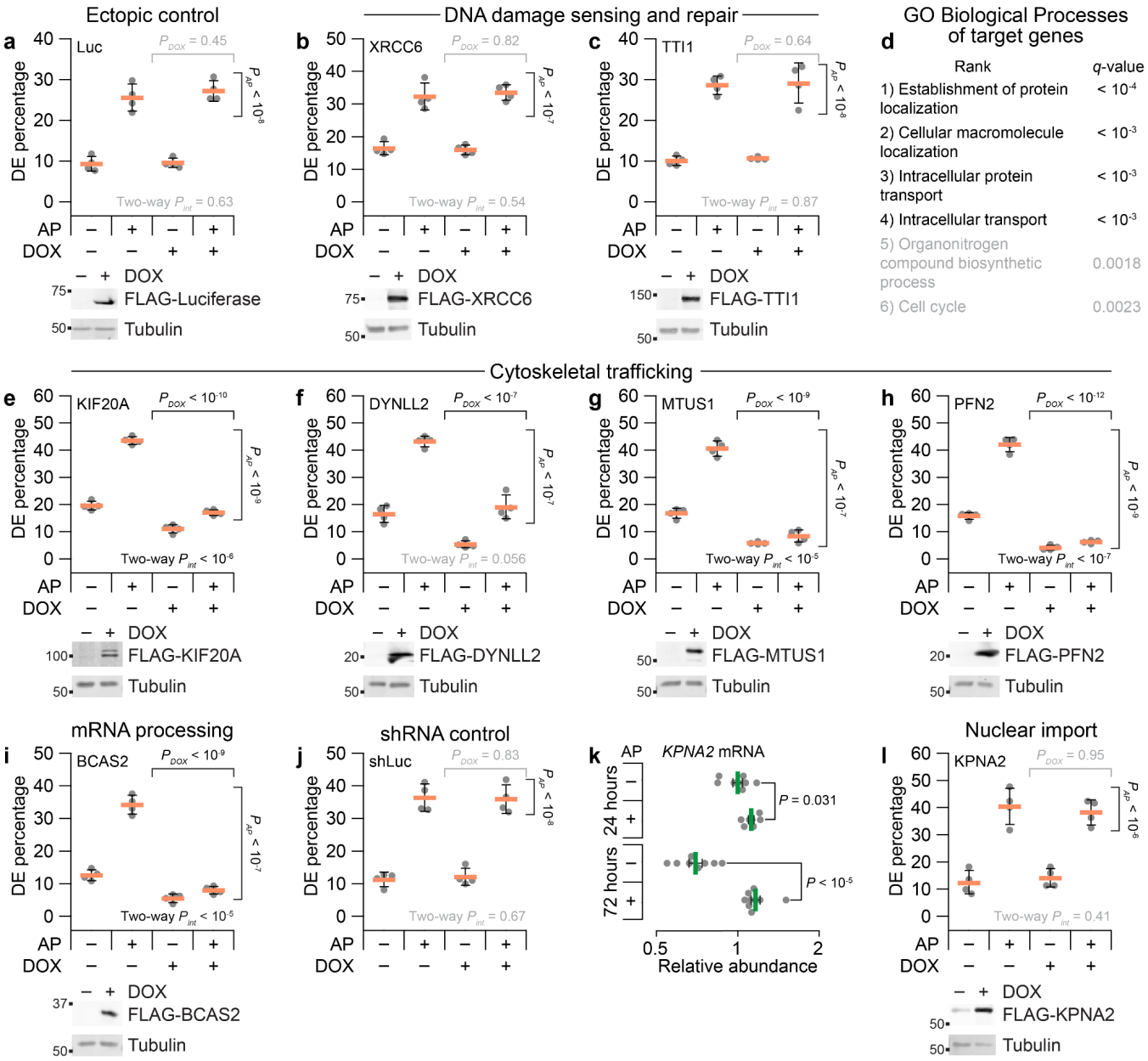

Extended Data Fig. 2 | Exclusion of alternative hypotheses regarding other fractionally induced candidates.

a, DE percentage for B2B1 cells stably expressing inducible FLAG-tagged luciferase as an ectopic expression control.

b, **c**, Candidates related to DNA damage sensing and repair do not affect DE penetrance induced by ErbB heterodimerization when ectopically expressed. B2B1 cells expressing inducible FLAG-tagged XRCC6 (**c**) or TTI1 (**d**) were used where indicated.

d, Enrichment analysis of gene ontology (GO) biological processes for the 97 candidate genes identified by stochastic frequency matching. False discovery rate-corrected *q*-values are shown for each biological process.

e–**h**, Candidates related to cytoskeletal trafficking inhibit DE penetrance induced by ErbB heterodimerization when ectopically expressed. B2B1 cells expressing inducible FLAG-tagged KIF20A (**e**), DYNLL2 (**f**), MTUS1 (**g**), or PFN2 (**h**) were used where indicated.

i, A candidate amplified in breast cancer[49] and involved in mRNA processing inhibits DE penetrance induced by ErbB heterodimerization when ectopically expressed. B2B1 cells expressing inducible FLAG-tagged BCAS2 were used.

j, DE percentage for B2B1 cells stably expressing inducible shRNA targeting luciferase (shLuc) as an shRNA control.
k, Quantitative PCR for *KPNA2* in B2B1 cells cultured in 3D for six days followed by addition of 0.5 μM AP21967 (AP) for 24 hours or 72 hours where indicated. Data are shown as the geometric mean (normalized to the 24-hour, minus-AP condition) ± log-transformed s.e. from n = 7–8 biological replicates. Differences in geometric means were assessed by two-sided t test after log transformation.
l, A regulator of nuclear import does not affect the penetrance of outgrowths induced by ErbB heterodimerization when ectopically expressed. B2B1 cells expressing inducible FLAG-tagged KPNA2 were used.
For **a–c**, **e–j**, and **l**, B2B1 cells stably expressing doxycycline (DOX)-inducible ectopic constructs were 3D cultured for 9–13 days with 0.5 μM AP added at Day 6 and/or 1 μg/ml DOX added at Day 5 where indicated. Data are shown as the arcsine transformed mean ± s.e. from n = 4 biological replicates where >100 outgrowths were scored per replicate. Differences by factor (DOX or AP) and two-factor interaction (int) were assessed by two-way ANOVA after arcsine transformation. Ectopic expression was confirmed by immunoblotting for FLAG with tubulin used as a loading control.

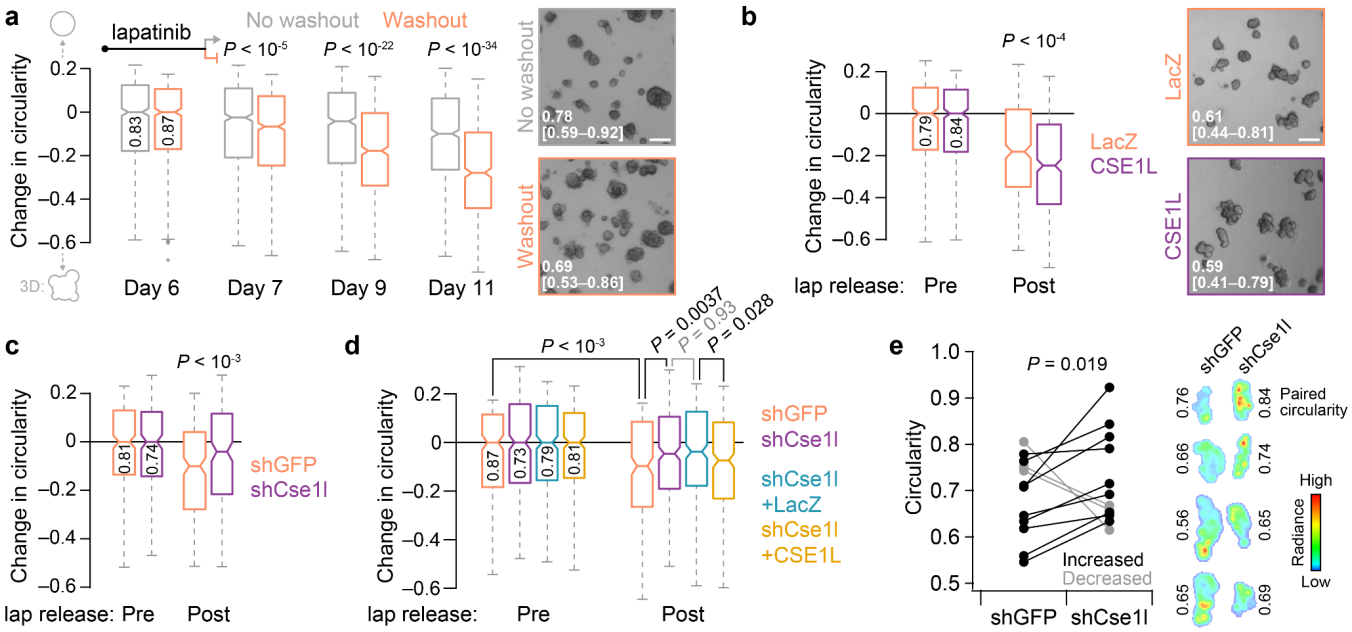

Fig. 3 | *Erbb2*-amplified mammary carcinoma cells develop Cse1l-dependent DEs in vitro and in vivo after lapatinib release.

a, Lapatinib release causes rapid and sustained loss of circularity in 3D-cultured mammary carcinoma cells with spontaneous *Erbb2* amplification. 3D phenotypes captured by the circularity metric are schematized in gray. Representative brightfield images of 3D cultures with or without lapatinib release for three days are shown on the right, with median circularity in the inset with interquartile range in brackets.

b, Ectopic induction of CSE1L exaggerates the loss of circularity following lapatinib (lap) release in 3D culture. Representative brightfield images of 3D cultures after four days of lapatinib release with or without ectopic CSE1L are shown on the right, with median circularity in the inset with interquartile range in brackets.

c, Inducible knockdown of Cse1l inhibits the loss of circularity following lapatinib (lap) release in 3D culture.

d, Inducible addback of human CSE1L reverts the circularity phenotype of shCse1l cells in 3D culture.

e, Paired change in circularity of lapatinib-released intraductal xenografts with or without knockdown of Cse1l. Representative bioluminescence images of contralateral xenografts from four animals are shown on the right alongside the estimated overall circularity of each tumor.

For **a–d**, TM15c6 cells stably expressing doxycycline (DOX)-inducible CSE1L (or LacZ control) or shCse1l (or shGFP control) were 3D cultured for five days in 2 μM lapatinib, followed by one day in 2 μM lapatinib + 1 μg/ml DOX (**b–d**, pre) and then 1 μg/ml DOX for 1–5 days (**a**), four days (**b**, post), three days (**c**, post), or one day (**d**, post). Circularities were analyzed for the upper 35th percentile of outgrowths by size [n = 636–924 (**a**), 334–476 (**b**), 173–242 (**c**), 227–316 (**d**) outgrowths from four biological replicates; shGFP and shCse1l cells were used twice independently in **c** and **d**]. Boxplots show the median reduction in circularity from the Day 6 time point (horizontal line, with Day 6 circularity reported vertically), estimated 95% confidence interval of the median (notches), interquartile range (box), and 1.5x the interquartile range from the box edge (whiskers). Differences between groups were assessed by two-sided rank sum test.

For **a** and **b**, the scale bar is 200 μm.

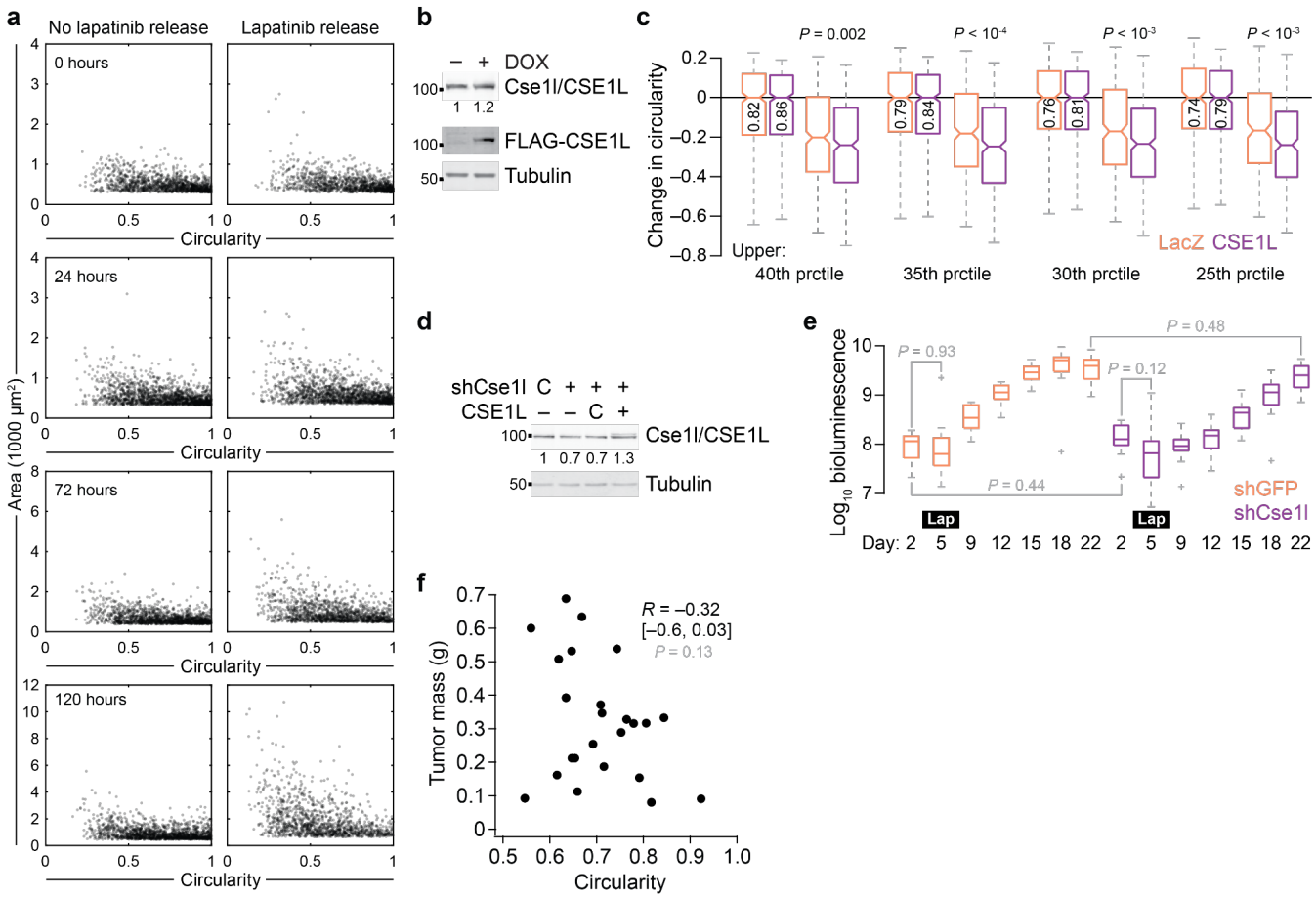

Extended Data Fig. 3 | 3D and in vivo characterization of TM15c6 cells with or without pharmacologic and genetic perturbations.

a, Changes in cross-sectional area upon lapatinib release do not noticeably skew changes in circularity. TM15c6 cells 3D cultured for five days in 2 μM lapatinib followed by release for the indicated time. Cross-sectional area and circularity were analyzed for all outgrowths (n = 1241–1755 outgrowths from four biological replicates).

b, Inducible ectopic expression of CSE1L confirmed by immunoblotting for total Cse1l/CSE1L and FLAG with tubulin used as a loading control. Inducible overexpression of total Cse1l/CSE1L was quantified relative to the minus-DOX control.

c, CSE1L-induced circularity phenotype is not sensitive to the choice of cross-sectional area thresholding. Circularities were analyzed for outgrowths above the indicated threshold by size (n = 504–1018 outgrowths from four biological replicates).

d, Inducible knockdown of Cse1l and addback of CSE1L. TM15c6 cells stably expressing inducible shCse1l or shGFP control (C) with or without inducible CSE1L or LacZ control (C) were treated with 1 μg/ml doxycycline for two days and immunoblotted for Cse1l/CSE1L with tubulin used as a loading control.

e, Dynamics of tumor bioluminescence in TM15c6 cells expressing shCse1l or shGFP control after inoculation at Day 0 and administration of 30 mg/kg lapatinib i.p. daily from Days 3–9 (n = 12 animals).

For **c** and **e**, boxplots show the median bioluminescence, interquartile range (box), estimated 95% confidence interval of the median (**c**, notches), 1.5x the interquartile range from the box edge (whiskers), and outliers (+). Differences between indicated groups were assessed by two-sided rank sum test with Šidák correction for multiple-hypothesis testing.

f, Tumor size is not significantly correlated with tumor circularity. Mass and circularity of excised tumors (n = 24 samples) were assessed by Pearson correlation (R) with 95% confidence interval and hypothesis testing for nonzero correlation estimated after Fisher Z transformation.

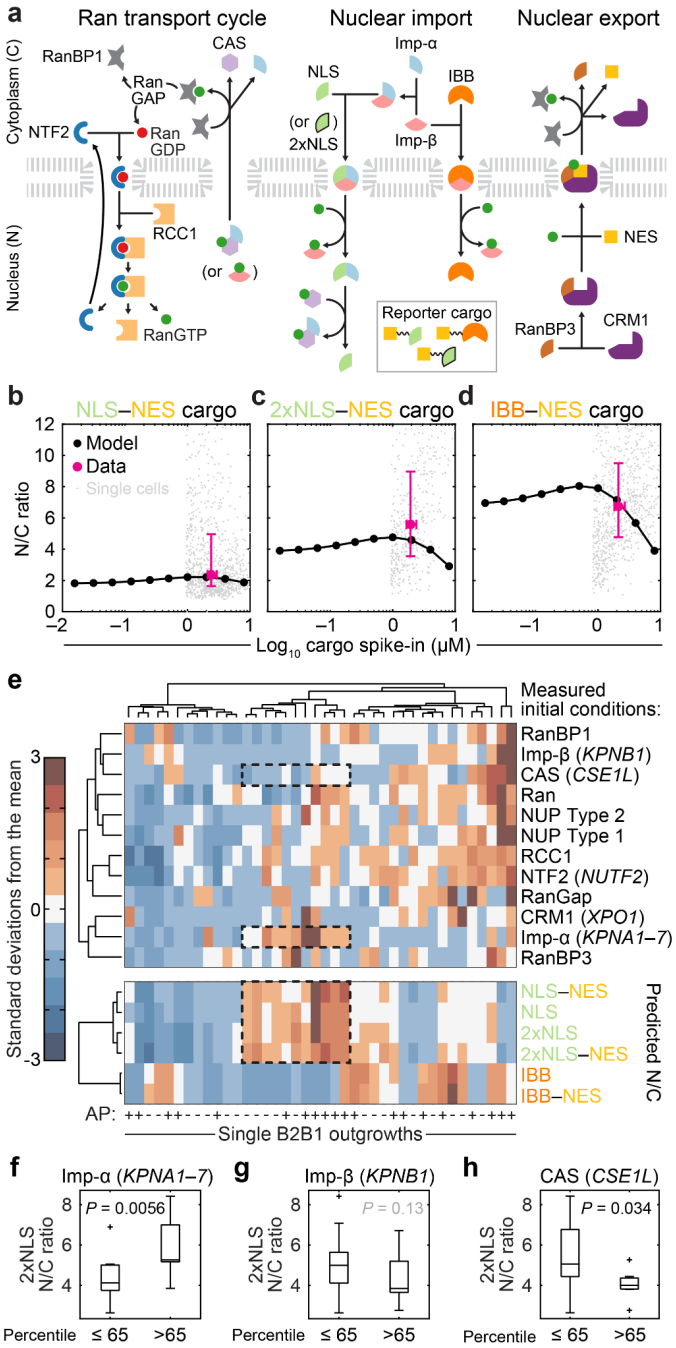

Fig. 4 | Long-term ErbB heterodimerization triggers divergent nucleocytoplasmic transport at the systems level.

a, Overview of an integrated systems model of nucleocytoplasmic transport adapted from Riddick and Macara[60, 61]. Symbols are introduced at first use according to the original naming scheme[60, 61]. Binding reactions are reversible, but arrows indicate the dominant direction of the reaction. Reporter cargos were engineered to fuse a nuclear export sequence (NES) with one of three import sequences: the nuclear localization sequence of simian virus 40 T antigen (NLS) or of cap-binding protein 80 (2xNLS), which bind to Imp-α/β heterodimers with different affinity, or the Imp-β-binding domain of KPNA2 (IBB), which binds directly to Imp-β. Full details on the model are available in Supplementary Note 1.

b–d, Calibration of the model to B2B1 initial conditions (Supplementary Note 1) accurately predicts steady-state accumulation of induced NLS–NES (**b**), 2xNLS–NES (**c**), and IBB–NES (**d**) in the nucleus (N) relative to the cytoplasm (C). Steady-state N/C ratios were predicted for each reporter induced from

0.01–10 μM (black) and compared to population-level estimates of reporter abundance measured by quantitative immunoblotting[110] and N/C ratios measured by immunofluorescence (magenta). Population-level data (magenta) are shown as the mean ± s.e. from n = 4 (**b,c**) or 3 (**d**) biological replicates on the x-axis and the median ± interquartile range from n = 1052 (**b**), 445 (**c**), or 861 (**d**) cells (gray; median-scaled along the x-axis to the population mean) collected from four biological replicates.

e, Outgrowth-specific predictions of steady-state N/C ratios from the model. Transcriptome-wide profiles from each B2B1 3D outgrowth with or without AP21967 (AP, upper) were used to scale the initial conditions of all model species (see Methods) and simulate the steady-state accumulation of 1 μM NLS, 2xNLS, or IBB import sequences with or without NES (lower). Model initial conditions and steady-state N/C ratios were hierarchically clustered separately by row and together by column with Ward's linkage after row standardization. Examples of high N/C states for NLS and 2xNLS are boxed alongside model species of interest.

f–h, Proportionately high expression of Imp-α and CAS, but not Imp-β, alters the steady-state accumulation of Imp-α/β-binding cargo. Predicted 2xNLS N/C ratio for n = 20 AP-treated B2B1 outgrowths split at the 65th percentile according to relative transcript abundance of *KPNA1–7* (**f**), *KPNB1* (**g**), or *CSE1L* (**h**). Boxplots show the median N/C ratio (horizontal line), interquartile range (box), 1.5x the interquartile range from the box edge (whiskers), and outliers (+). Differences between groups were assessed by one-sided rank sum test.

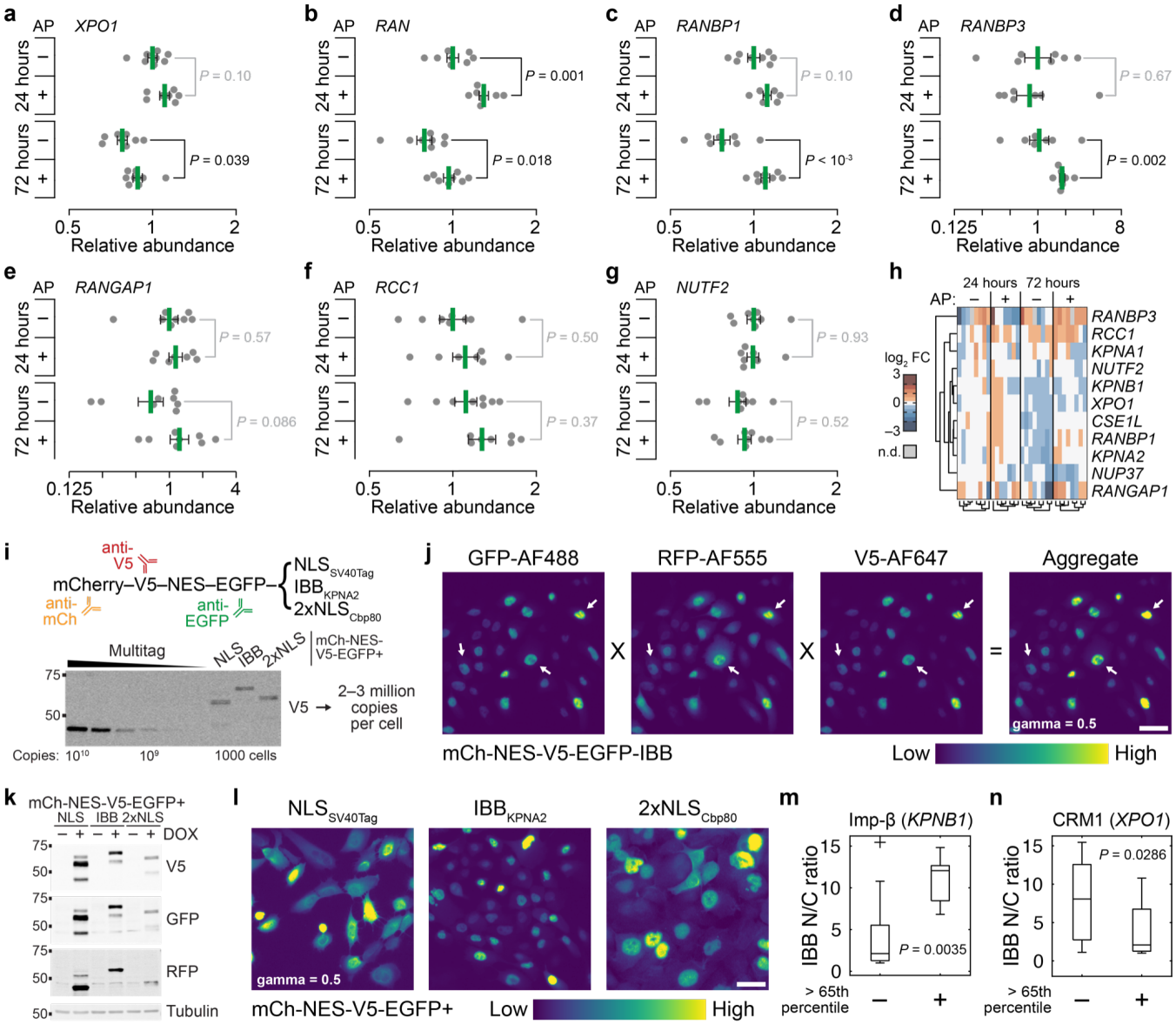

Extended Data Fig. 4 | Motivation, testing, and use of a nucleocytoplasmic transport model.
a–g, Quantitative PCR for *XPO1* (**a**), *RAN* (**b**), *RANBP1* (**c**), *RANBP3* (**d**), *RANGAP1* (**e**), *RCC1* (**f**), and *NUTF2* (**g**) in B2B1 cells cultured in 3D for six days followed by addition of 0.5 μM AP21967 (AP) for 24 hours or 72 hours where indicated. Data are shown as the geometric mean (normalized to the 24-hour, minus-AP condition) ± log-transformed s.e. from n = 7–8 biological replicates. Differences in geometric means were assessed by two-sided t test after log transformation.
h, Replicate-by-replicate clustergram of the quantitative PCR data from Fig. 2g–j, Extended Data Fig. 2k, and Extended Data Fig. 4a–g. Data were normalized to the geometric mean of the 24-hour, minus-AP condition for each gene and row clustered by Euclidean distance with Ward's linkage. Individual replicate groups were column clustered separately
i, Design and quantification of the tandem cargo reporters. mCherry (mCh), V5, and EGFP were used as epitope tags to localize the steady-state accumulation of different localization sequences paired with the same NES. Absolute copy-number quantification was performed with recombinant V5-containing Multitag[111].
j, Image math for Alexa Fluor (AF)-based immunolocalization of GFP, RFP (crossreactive with mCh), and V5 to estimate full-length tandem cargo reporter.
k, Inducible expression and cleavage products of tandem cargo reporters. B2B1 cells expressing inducible mCh-NES-V5-EGFP tagged with $NLS_{SV40Tag}$, IBB_{KPNA2}, or $2xNLS_{Cbp80}$ were induced with 1 μg/ml

doxycycline (DOX) for 6 hours were immunoblotted for the indicated epitopes with tubulin used as a loading control.

l, Representative image math immunolocalization of the indicated tandem cargo reporters after DOX induction for 6 hours. Quantification is summarized in Fig. 3b–d.

m, **n**, Proportionately high expression of Imp-β and CRM1 alters the steady-state accumulation of Imp-β-binding cargo. Predicted IBB nuclear/cytoplasmic (N/C) ratio for n = 20 AP-treated B2B1 outgrowths split at the 65th percentile according to relative transcript abundance of *KPNB1* (**e**), or *XPO1* (**f**). Boxplots show the median N/C ratio (horizontal line), interquartile range (box), 1.5x the interquartile range from the box edge (whiskers), and outliers (+). Differences between groups were assessed by a one-sided rank sum test.

For **j** and **l**, aggregate images are displayed with image gamma = 0.5, and the scale bar is 20 μm.

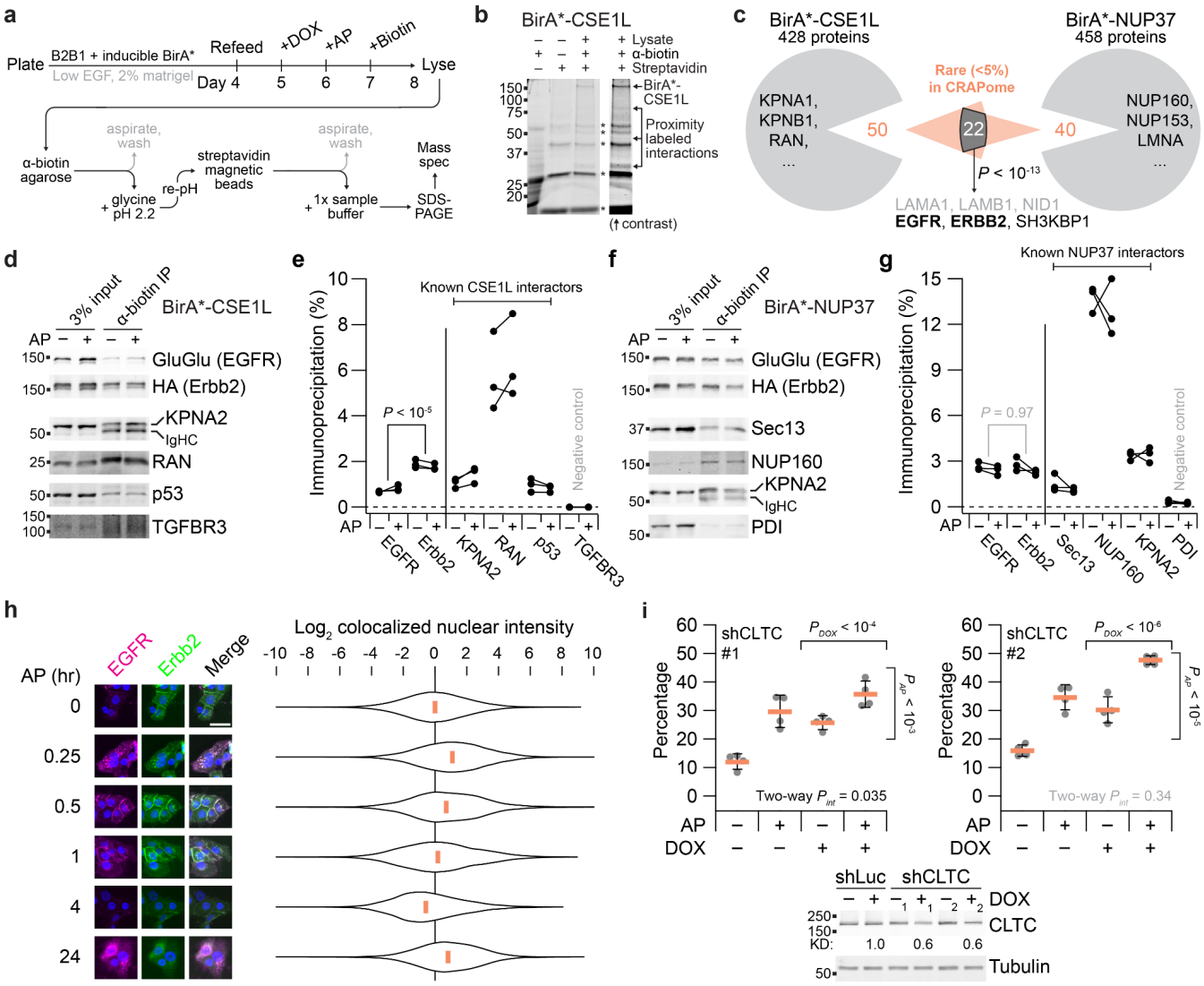

Fig. 5 | CSE1L–NUP37 proximity labeling implicates a role for nucleocytoplasmic transport of EGFR–Erbb2.

a, Overview experimental schema for proximity labeling. B2B1 cells expressing inducible FLAG-tagged BirA*-CSE1L or BirA*-NUP37 were plated and overlaid as described[68], induced with 1 μg/ml DOX, heterodimerized with 0.5 μM AP, and labeled with 50 μM biotin on the indicated days and lysed after 24 hours of labeling. Proximity-labeled extracts were immunopurified with anti-biotin agarose beads[112], glycine eluted, neutralized, and second-step purified on streptavidin magnetic beads before sample buffer elution, SDS-PAGE, and mass spectrometry.

b, Two-step affinity purification of proximity-labeled extracts. SDS-PAGE of sample buffer-treated anti-biotin agarose beads, streptavidin magnetic beads, or extracts enriched through the two-step procedure. Non-specific bands from the terminal elution are indicated with asterisks.

c, Summary of proximity-labeled proteins identified by mass spectrometry. Representative BioGRID interactors identified from each study are listed along with a subset of shared targets predicted to be highly specific according to their rarity in the CRAPome database[70]. Overlap significance was determined by hypergeometric test. Residual matrigel contaminants are listed in gray. ERBB2 peptides were indistinguishable from rat Erbb2.

d–g, Replicated target validation for BirA*-CSE1L and BirA*-NUP37. Anti-biotin immunoprecipitates of proximity-labeled extracts from B2B1 cells expressing inducible FLAG-tagged BirA*-CSE1L (**d**) or BirA*-NUP37 (**f**) and treated with or without 0.5 μM AP for 24 hours before biotinylation for 24 hours were immunoblotted for the indicated targets and quantified from n = 3 paired biological replicates by

densitometry (**e,g**). Differences in overall EGFR and Erbb2 proximity labeling were assessed by two-way ANOVA with replication.

h, Colocalized EGFR–Erbb2 puncta accumulate in the nucleus within one hour and at 24 hours after heterodimerization. B2B1 cells were plated on coverslips, treated with 0.5 μM AP for the indicated times, and immunostained for GluGlu tag (EGFR, magenta) and HA tag (Erbb2, green) with DAPI counterstain for nuclei (blue). Scale bar is 20 μm. Violin plots show the median and distribution of nuclear-masked, colocalized GluGlu–HA pixel intensities from n = 276–396 cells (92,485–107,009 pixels) at each time point.

i, Knockdown of clathrin-dependent endocytosis elevates the basal penetrance of the DE phenotype. B2B1 cells expressing inducible shCLTC were 3D cultured for 10 days with 0.5 μM AP added at Day 6 and/or 1 μg/ml DOX added at Day 5 where indicated. Data are shown as the arcsine transformed mean ± s.e. from n = 4 biological replicates where >150 outgrowths were scored per replicate. Differences by factor (DOX or AP) and two-factor interaction (int) were assessed by two-way ANOVA after arcsine transformation. Inducible knockdown was quantified relative to the paired no DOX control with tubulin used as a loading control.

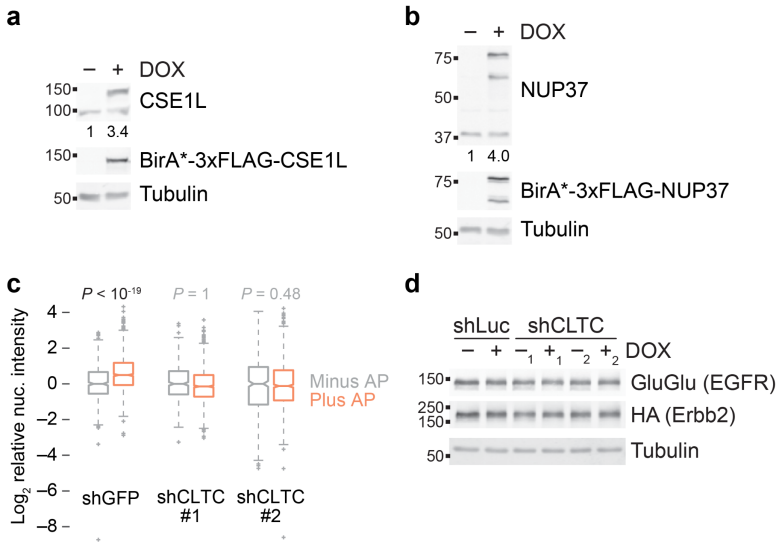

Extended Data Fig. 5 | Extended data related to CSE1L–NUP37 proximity labeling and CLTC knockdown.

a, b, Induction of ectopic BirA*-CSE1L (**a**) or BirA*-NUP37 (**b**) relative to endogenous protein. Inducible expression was compared relative to the no DOX control with tubulin used as a loading control.

c, CLTC knockdown inhibits the internalization of EGFR–Erbb2 heterocomplexes. B2B1 cells expressing the indicated shRNAs were plated on coverslips and induced with 1 μg/ml DOX for 48 hours before treatment with 0.5 μM AP for 15 minutes and immunostaining for GluGlu and HA tags. Boxplots show the normalized nuclear intensity (relative to minus AP), interquartile range (box), estimated 95% confidence interval of the median (notches), 1.5x the interquartile range from the box edge (whiskers), and outliers (+) from n = 433–1146 cells of two or four biological replicates. Differences between AP groups were assessed by one-sided rank sum test.

d, CLTC knockdown does not alter long-term abundance of EGFR or Erbb2 chimeras. B2B1 cells expressing the indicated shRNAs were immunoblotted for GluGlu and HA tags with tubulin used as a loading control.

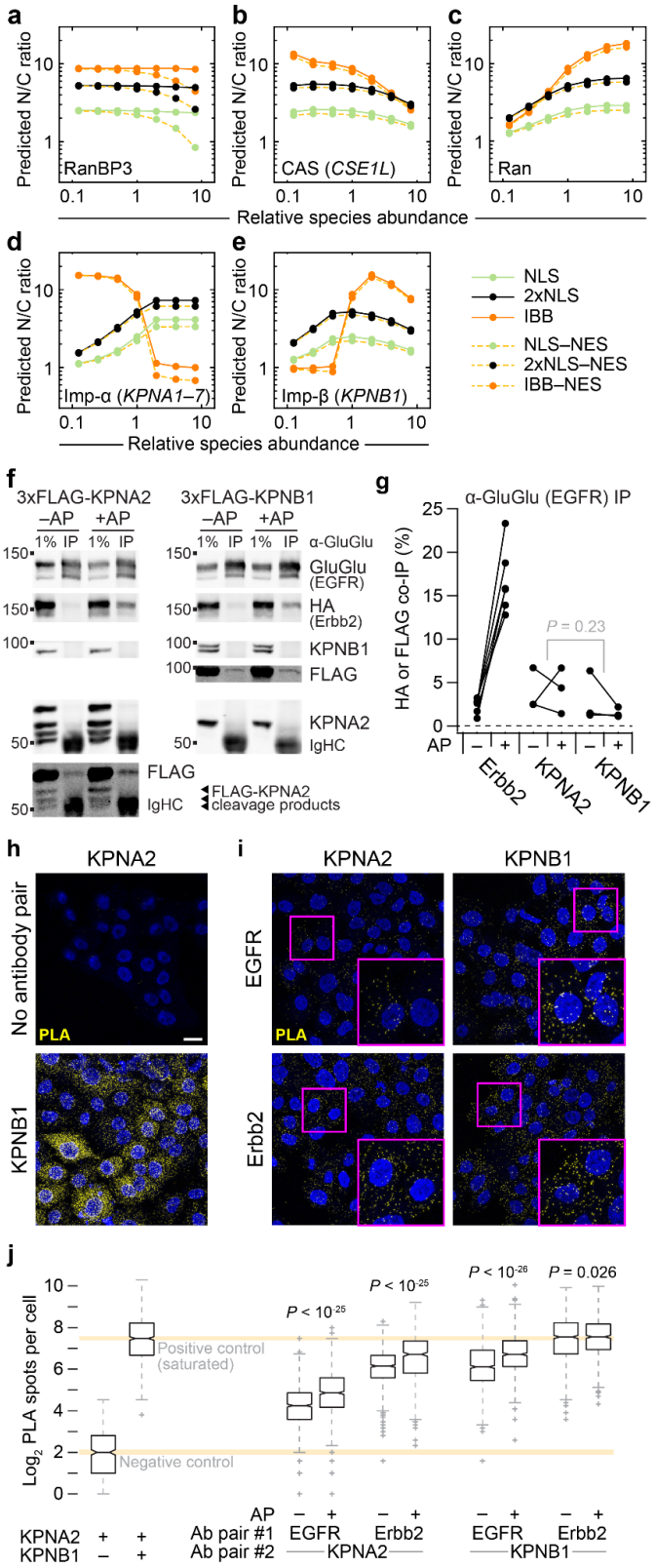

Fig. 6 | EGFR and Erbb2 bind karyopherins of the classical nuclear-import family.
a–e, Predicted sensitivity of the systems model to starting protein concentrations of RanBP3 (**a**), CAS (**b**), Ran (**c**), Imp-α (**d**), and Imp-β (**e**). Protein abundances are scaled relative to the concentrations used in the base model (Supplementary Table 4). Steady-state nuclear-to-cytoplasmic (N/C) ratios are shown for 1 μM of the representative cargo described in Fig. 4a.

f, g, EGFR inducibly associates with Erbb2 and constitutively associates with KPNA2 and KPNB1. B2B1 cells expressing doxycycline (DOX)-inducible 3xFLAG-KPNA2 or 3xFLAG-KPNB1 were induced with 1 μg/ml DOX for 24 hours and then treated with or without 0.5 μM AP for one hour before lysis and GluGlu immunoprecipitation of the EGFR chimera. Samples were immunoblotted for the indicated targets (**f**) and quantified from n = 3 paired biological replicates by densitometry relative to the amount of immunoprecipitated EGFR chimera (**g**).
h, i, ErbB interactions with karyopherins confirmed by proximity ligation assay (PLA). B2B1 cells were plated and stained with the indicated antibody combinations. Negative and positive controls (**h**) were KPNA2 alone and KPNA2:KPNB1 respectively. Experimental antibody pairings (**i**) combined EGFR and Erbb2 chimeras with KPNA2 or KPNB1 as indicated. Scale bar is 20 μm.
j, Quantification of PLA spots in control samples and B2B1 cells treated with or without 0.5 μM AP for 24 hours and stained with the indicated antibody combinations. Boxplots show the median PLA spots per cell (horizontal line), interquartile range (box), estimated 95% confidence interval of the median (notches), 1.5x the interquartile range from the box edge (whiskers), and outliers (+) from n = 465–985 cells from 16 confocal image stacks across two coverslips per condition. Differences between groups were assessed by two-sided KS test with Bonferroni correction.

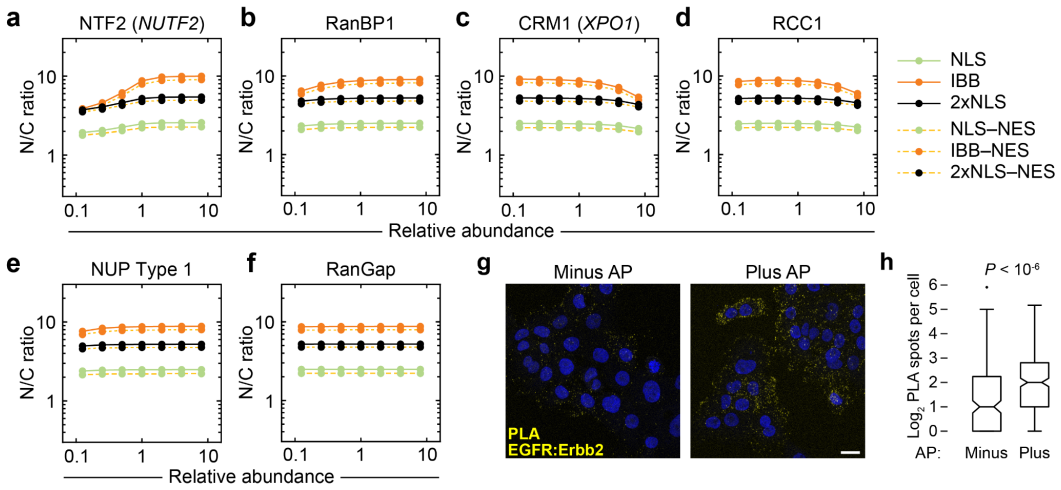

Extended Data Fig. 6 | Extended sensitivity analysis of the model and validation of the proximity ligation assay.

a–f, Predicted sensitivity of the systems model to starting protein concentrations of NTF2 (**a**), RanBP1 (**b**), CRM1 (**c**), RCC1 (**d**), total NUP (**e**), and RanGap (**f**). Protein abundances are scaled relative to the concentrations used in the base model (Supplementary Table 4). Steady-state nuclear-to-cytoplasmic (N/C) ratios are shown for 1 μM of the representative cargo described in Fig. 4a.

g, The proximity ligation assay detects regulated protein-protein interactions. B2B1 cells were treated with or without 0.5 μM AP for 15 minutes and costained for interaction between the EGFR and Erbb2 chimeras. Scale bar is 20 μm.

h, Quantification of PLA spots in B2B1 cells treated with or without 0.5 μM AP and stained as in (**g**). Boxplots show the median PLA spots per cell (horizontal line), interquartile range (box), estimated 95% confidence interval of the median (notches), 1.5x the interquartile range from the box edge (whiskers), and outliers (+) from n = 195–272 cells from eight confocal image stacks on one coverslip per condition. Differences between groups were assessed by two-sided KS test with Bonferroni correction.

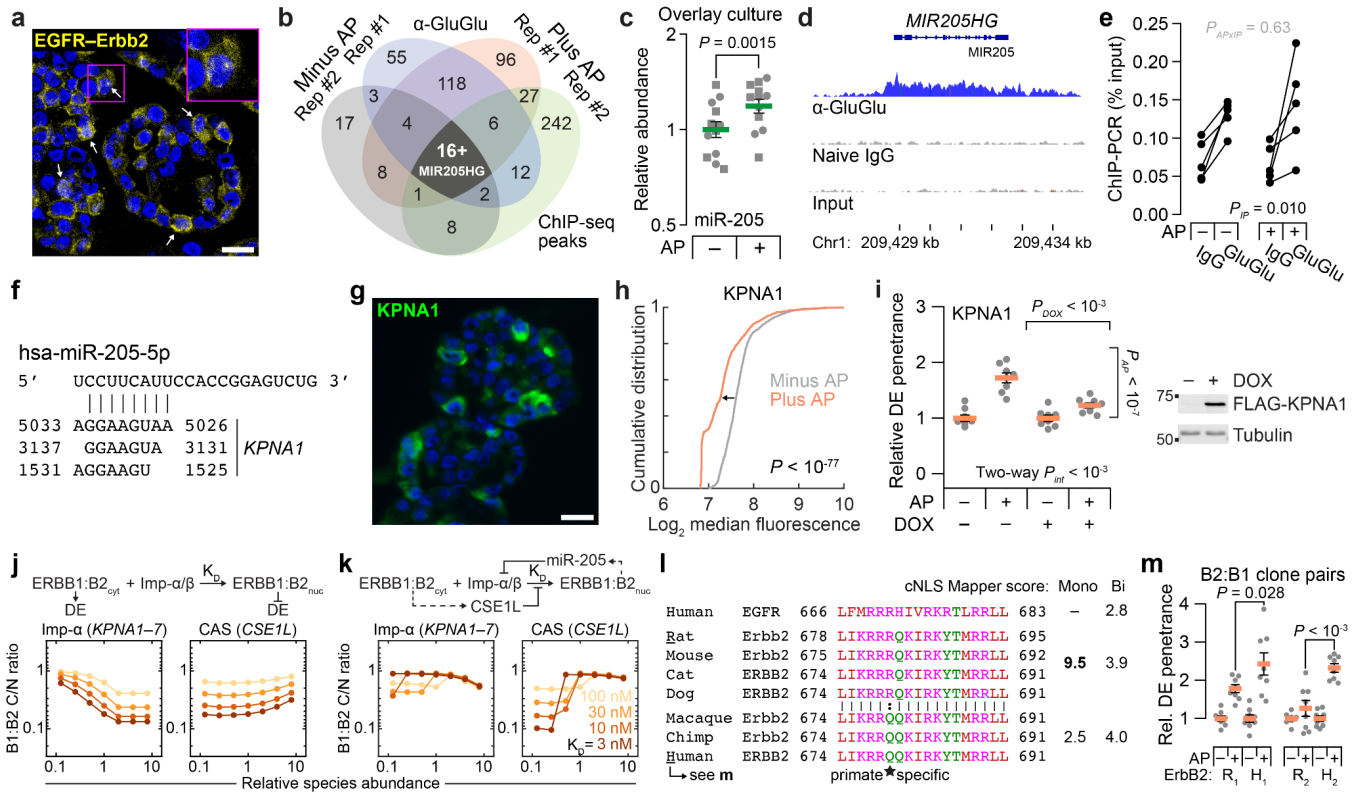

Fig. 7 | Nuclear ErbBs induce a miR-205–KPNA1 negative feedback that causes switchlike sensitivity to CSE1L abundance in a species-specific manner.

a, Colocalized EGFR:Erbb2 staining in the nucleus of B2B1 cells cultured in 3D for six days followed by addition of 0.5 μM AP for 24 hours. Confocal images of GluGlu and HA immunoreactivities were quantile-normalized and geometrically averaged (yellow) and nuclei were counterstained with DAPI (blue). The inset shows an enlarged view of a cell with nuclear EGFR:Erbb2.

b, Venn diagram of genomic peaks detected by ChIP-seq for EGFR chimera in B2B1 cells overlay cultured for six days ± 0.5 μM AP for 24 hours in biological duplicate.

c, TaqMan quantification of miR-205 from B2B1 cells overlay cultured for six days followed by addition of 0.5 μM AP for 24 hours. Data are shown as the geometric mean (normalized to the 24-hour, minus-AP condition) ± log-transformed s.e. from n = 12 biological replicates collected in two batches (circles, squares) and measured in technical duplicates. Differences in geometric means were assessed by two-way ANOVA after log transformation. AP was used as a fixed effect and technical replicates were used as a random effect.

d, Binding of EGFR chimera to the *MIR205HG* locus relative to naive IgG.

e, ChIP-quantitative PCR (qPCR) for the *MIR205HG* locus in B2B1 cells overlay cultured for six days ± 0.5 μM AP for 24 hours where indicated. Chromatin was immunoprecipitated with GluGlu epitope tag or naive IgG and quantified relative to input chromatin. Differences in means were assessed by three-way ANOVA with immunoprecipitating antibody (IP), AP, and biological replicates used as fixed effects. Tests are shown for the IP effect and the APxIP interaction effect.

f, TargetScan[90] predictions of miR-205 binding sites within the 3' untranslated region of *KPNA1*. The 1525–1531 site is broadly conserved.

g, Immunofluorescence staining for KPNA1 (green) in cryosections from B2B1 cells cultured in 3D for six days followed by addition of 0.5 μM AP for 24 hours. Nuclei were counterstained with DAPI (blue).

h, Quantification of median KPNA1 immunoreactivity in cryosections from B2B1 cells cultured in 3D for six days ± 0.5 μM AP for an additional 24 hours. Data are shown as the cumulative distribution from n = 894 (minus AP) or 870 (plus AP) cells from 3D outgrowths pooled from four biological replicates. Differences in distribution were assessed by two-sided KS test.

i, Ectopic induction of KPNA1 affects the penetrance of outgrowths induced by ErbB heterodimerization. B2B1 cells stably expressing doxycycline (DOX)-inducible FLAG-tagged KPNA1 were 3D cultured for 11 days with 0.5 μM AP and/or 1 μg/ml DOX added at Day 5 where indicated. DCIS escape (DE) frequencies were normalized to the minus-AP, minus-DOX condition and are shown as the mean ± s.e. from n = 8 biological replicates where >70 outgrowths were scored per replicate. Differences by factor (DOX or AP) and two-factor interaction (int) were assessed by two-way ANOVA. Ectopic expression was confirmed by immunoblotting for FLAG with tubulin used as a loading control.
j,k, Sensitivity of the existing systems model (**j**) to Imp-α and CSE1L abundance for ErbB heterodimers acting as classical cargo for Imp-α:Imp-β heterodimers with the indicated dissociation constant (K_D). Cytoplasmic (cyt) heterodimers are presumed to promote DCIS escape (DE), whereas nuclear heterodimers suppress DE (Fig. 2a,e, 5i, 7i). The revised model (**k**) includes linear negative feedbacks involving CSE1L (Fig. 2g, 4h) and miR-205 (Fig. 7b–h). Simulations were performed with 1 μM cargo.
l, Alignment of the tripartite nuclear localization sequence[76] of ErbB orthologs among primates and non-primates. Groups are shown along with bioinformatic scores as monopartite (Mono) or bipartite (Bi) nuclear localization sequences for the surrounding region according to cNLS Mapper[93].
m, Weaker nuclear localization of human ERBB2 coincides with increased DE penetrance. Paired B2:B1 clones expressing similar levels of human EGFR and either rat Erbb2 (R_1, R_2) or human ERBB2 (H_1, H_2) were 3D cultured for 10 days with 0.5 μM AP added at Day 5 where indicated. DE frequencies were normalized to the minus-AP condition for each clone and are shown as the mean ± s.e. from n = 8 biological replicates where >150 outgrowths were scored per replicate. Differences in AP-induced DE penetrance were assessed by one-sided t test.
For **a** and **g**, the scale bar is 20 μm.

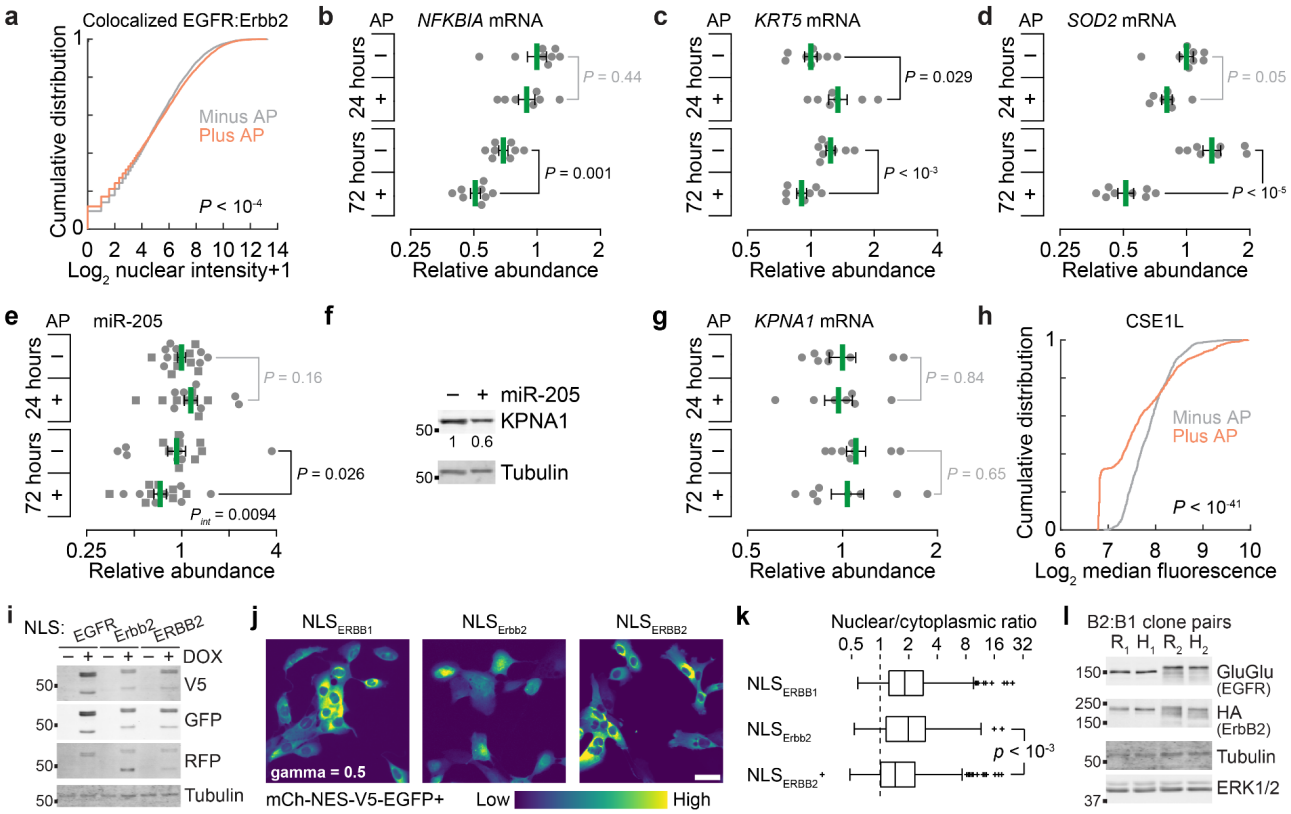

Extended Data Fig. 7 | Extended data related to genomic loci bound by chimeric EGFR, controls for miR-205, and comparisons of ErbBs from primates and rodents.

a, Integrated intensity of colocalized EGFR:Erbb2 staining in the nucleus of B2B1 cells cultured in 3D for six days with or without 0.5 μM AP for an additional 24 hours. Differences in distributions were assessed by two-sided KS test.

b–e, Quantitative PCR for *NFKBIA* (**b**), *KRT5* (**c**), *SOD2* (**d**), and miR-205 (**e**) in B2B1 cells cultured in 3D for six days followed by addition of 0.5 μM AP21967 (AP) for 24 hours or 72 hours where indicated.

f, miR-205 suppresses KPNA1. 293T cells were transfected with miR-205 precursor or negative control for 48 hours and immunoblotted for KPNA1 with tubulin used as a loading control.

g, Quantitative PCR for *KPNA1* in B2B1 cells cultured in 3D for six days followed by addition of 0.5 μM AP21967 (AP) for 24 hours or 72 hours where indicated.

h, Quantification of median CSE1L immunoreactivity in cryosections from B2B1 cells cultured in 3D for six days ± 0.5 μM AP for an additional 24 hours. Data are shown as the cumulative distribution from n = 894 (minus AP) or 870 (plus AP) cells from 3D outgrowths pooled from four biological replicates. Differences in distribution were assessed by two-sided KS test.

i, Inducible expression of ErbB tandem cargo reporters. B2B1 cells expressing inducible mCh-NES-V5-EGFP tagged with NLS_{EGFR}, NLS_{Erbb2}, or NLS_{ERBB2} were induced with 1 μg/ml doxycycline (DOX) for 6 hours were immunoblotted for the indicated epitopes with tubulin used as a loading control.

j,k, Representative image math immunolocalization (**j**) and quantification (**k**) of the indicated tandem cargo reporters after DOX induction for 6 hours. Boxplots show the median N/C ratio (horizontal line), interquartile range (box), 1.5x the interquartile range from the box edge (whiskers), and outliers (+) from n = 283 (NLS_{ERBB1}), 285 (NLS_{Erbb2}), and 333 (NLS_{ERBB2}) cells collected from four biological replicates. Differences were assessed by two-sided rank sum test. For **j**, the scale bar is 20 μm.

l, Characterization of ErbB clones expressing human ERBB2 or rat Erbb2. Protein extracts were immunoblotted for GluGlu and HA epitope tags with tubulin and ERK1/2 used as loading controls.

For **b–e** and **f**, data are shown as the geometric mean (normalized to the 24-hour, minus-AP condition) ± log-transformed s.e. from n = 7–8 biological replicates. Differences in geometric means were assessed by two-sided t test after log transformation.

Supplementary Table 1 | Predicted regulatory heterogeneities in 3D-cultured B2B1 cells minus AP heterodimerizer.

Supplementary Table 2 | Predicted regulatory heterogeneities in 3D-cultured B2B1 cells plus AP heterodimerizer.

Supplementary Table 3 | Transcript heterogeneities and estimated expression frequencies for high-priority targets and candidates for the DE phenotype.

Supplementary Table 4 | Initial conditions and rate constants for the systems model of nucleocytoplasmic transport.

Supplementary Table 5 | Proximity labeled proteins in B2B1 cells expressing BirA*-CSE1L or BirA*-NUP37.

Supplementary Table 6 | Genomic loci bound by chimeric EGFR in B2B1 cells with or without AP heterodimerizer.

Supplementary Table 7 | Cloning details, PCR primers, and antibodies.

Supplementary Video 1 | Brightfield time lapse of B2B1 outgrowths treated with AP heterodimerizer for the indicated times. Scale bar is 100 µm.

Supplementary Note 1 | Reconstruction of the nucleocytoplasmic transport model.

METHODS

Plasmids.

ErbB chimeras. For EGFR, pBabe NGFR-FRB-GluGlu neo was prepared by triple ligation of pBabe neo digested with EcoRI–SalI, NGFR (1–274) PCR amplified and digested with MfeI–SpeI, and FRB-GluGlu PCR amplified and digested with SpeI–SalI. Next, pBabe NGFR-EGFR-FRB-GluGlu neo was prepared by ligating pBabe NGFR-FRB-GluGlu neo digested with SpeI and EGFR (624–1165) PCR amplified and digested with XbaI–SpeI.

For Erbb2, pBabe NGFR-2xFKBP-HA hygro was prepared by triple ligation of pBabe hygro digested with EcoRI–SalI, NGFR (1–274) PCR amplified and digested with MfeI–XbaI, and 2xFKBP-HA PCR amplified and digested with XbaI–SalI. Next, pBabe NGFR-Erbb2-2xFKBP-HA hygro was prepared by ligating pBabe NGFR-2xFKBP-HA hygro digested with XbaI and Erbb2 (680–1259) PCR amplified and digested with SpeI.

For ERBB2, pBabe NGFR-ERBB2-2xFKBP-HA hygro was prepared by quadruple ligation of pBabe hygro digested with BamHI–SalI, NGFR (1–274) PCR amplified and digested with BamHI–XbaI, ERBB2 (676–1255) PCR amplified and digested with XbaI–MfeI, and 2xFKBP-HA PCR amplified and digested with MfeI–SalI.

Inducible shRNA. Doxycycline-regulated shRNAs from the RNAi Consortium were cloned exactly as described previously[57]: shNUP37 v1 (TRCN0000152222), shNUP37 v2 (TRCN0000151312), shCSE1L v1 (TRCN0000061790), shCSE1L v2 (TRCN0000061792), shCse1l (TRCN0000217479), shCLTC v1 (TRCN0000380642), shCLTC v2 (TRCN0000379759). Control shRNAs targeting luciferase or GFP were previously described (Addgene #83092, #83085) [57].

Inducible ectopic expression. Doxycycline-regulated expression of BirA*, BCAS2, CSE1L, DYNLL2, KIF20A, KPNA1, KPNB1, MTUS1, NUP37, PFN2, TTI1, and XRCC6 were cloned by PCR into pEN_TT_miRc2 3xFLAG (Addgene #83274)[113]. For KPNA2, a linker was cloned into pEN_TT_miRc2 3xFLAG (Addgene #192305), and KPNA2 into pEN_TT_miRc2 3xFLAG linker. For NPIPB11-FLAG, a linker was cloned into pEN_TT_miRc2 (Addgene #25752), and NPIPB11-FLAG was cut with KpnI and SphI and cloned into pEN_TT_miRc2 linker. For proximity labeling, CSE1L and NUP37 were cloned by PCR into pEN_TT_miRc2 3xFLAG-BirA* (Addgene #192307). Full cloning details are available in Supplementary Table 7. All pEN_TT donor vectors were LR recombined with either pSLIK zeo (for B2B1 cells; Addgene #25736) or pSLIK neo (for TM15c6 cells; Addgene #25735) [114] for lentiviral packaging. pSLIK 3xFLAG-Luciferase zeo (for B2B1 cells; Addgene #136533) or pSLIK 3xFLAG-LacZ neo (for TM15c6 cells; Addgene #83105) was used as a control[113]. All plasmids were verified by sequencing and deposited with Addgene (#192291–#192348).

Tandem cargo reporters. pEN_TT mCh-V5-NES-EGFP was prepared by triple ligation of pEN_TT_miRc2 digested with SpeI–MfeI, mCherry-ggtaagcctatccctaaccctctcctcggtctcgattctacg (V5) PCR amplified (without stop codon) and digested with SpeI–AgeI, and ttagccttgaaattagcaggtcttgatatc (NES)-EGFP-ggtacc (KpnI) PCR amplified (without stop codon) and digested with AgeI–MfeI. Tandem cargo reporters were then prepared by ligating pEN_TT mCh-V5-NES-EGFP digested with KpnI–MfeI and one of six nuclear localization sequences prepared with a stop codon and KpnI–MfeI overhangs: i) $NLS_{SV40Tag}$—ccaaaaaagaagagaaaggta; ii) $2xNLS_{Cbp80}$—atgtcgcggaggcggcacagctacgagaacgatggtggacaacctcacaaaaggaggaagacgtct; iii) IBB_{KPNA2}—KPNA2 (1-70); iv) NLS_{EGFR}—cgaaggcgccacatcgttcggaagcgcacgctgcggagg; v) NLS_{Erbb2}—aaacgaaggagacagaagatccggaagtatacgatgcgtagg; vi) NLS_{ERBB2}—aaacgaaggcagcagaagatccggaagtatacgatgcgtagg. All reporters were LR recombined with pSLIK zeo (Addgene #25736) for lentiviral packaging.

Cell lines and clones. For ErbB chimeras, MCF10A-5E cells[33] were transduced with pBabe NGFR-EGFR-FRB-GluGlu neo, selected with 300 µg/ml G418 (Sigma, A1720) until control plates had cleared, and cloned by limiting dilution in 96-well plates to yield a founding B1 clone. B2B1 cells were isolated by transducing the B1 clone with pBabe NGFR-Erbb2-2xFKBP-HA hygro, selecting with 10 µg/ml

hygromycin (Sigma, H0654) until control plates had cleared, and cloning by limiting dilution into 96-well plates. Paired human-rat clones were prepared by transducing the B1 clone with either pBabe NGFR-Erbb2-2xFKBP-HA hygro or pBabe NGFR-ERBB2-2xFKBP-HA hygro at titers adjusted to yield comparable HA expression at the population level. Then, polyclonal lines were surface labeled with NGFR antibody (NeoMarkers, MS-394-P0) and R-Phycoerythrin (PE)-conjugated goat-anti-mouse (Jackson ImmunoResearch, 115-116-146; 1:200 dilution), flow sorted into 96-well plates, and clones were screened for comparable receptor abundance by GluGlu and HA immunoblotting. TM15c6 cells (kindly provided by W.J. Muller)[51-53] were transduced with pLenti PGK V5-luciferase (w528-1) blast (Addgene #19166)[115] and selected with 10 µg/ml blasticidin (Thermo Fisher, R21001) until control plates had cleared. HeLa cells used to calibrate the original nucleocytoplasmic transport model (kindly provided by I.G. Macara) were cultured in DMEM plus 5% fetal bovine serum, 5% newborn calf serum, and 1x penicillin-streptomycin.

Viral transduction and selection. Lentiviral packaging, transduction, and selection with 300 µg/ml G418 (Sigma, A1720) or 25 µg/ml zeocin (Invitrogen, 46-0509) were performed exactly as described previously[68].

3D culture. *Receptor activation.* For B2B1 cells and human-rat clones, cells were plated on growth factor-reduced matrigel (Corning, 354230) and re-fed every four days as previously described[116]. On Day 6, cultures were spiked with 0.5 µM AP21967 (Takara, 635057) or 0.1% ethanol vehicle, and these perturbations were retained in the culture medium during subsequent refeeds. For TM15c6 cells, cells were plated on growth factor-reduced matrigel (Corning, 354230) in growth medium (DMEM medium (Gibco) plus 5% fetal bovine serum, 5 µg/ml insulin, 1 µg/ml hydrocortisone, 5 ng/ml EGF, 35 µg/ml bovine pituitary extract, and 50 µg/ml Gentamicin) supplemented with 2% matrigel + 2 µM lapatinib (MedChemExpress, HY-50898) and refed on Day 4. On Day 6, cultures were refed with growth medium + 2% matrigel and refed this way every four days thereafter.

Phenotype scoring. For B2B1 cells and human-rat clones, DEs were scored manually as 3D structures with at-least three lobes, excluding bi-lobed structures that could arise from two cells seeded next to one another. Total counts were collected by digital image acquisition and segmentation[117]. For TM15c6 cells, 3D structures were digitally acquired and segmented to estimate circularity thresholded by overall size.

Cryoembedding. B2B1 cells were not compatible with prior immunostaining protocols[68, 116] because outgrowths detached from the matrigel during the fixation step. Therefore, after washing briefly with PBS and fixing with 3.7% paraformaldehyde for 20 minutes at room temperature, the detached outgrowths from four wells were pooled, pelleted in a microcentrifuge tube, and washed three times in PBS for five minutes each. Fixed outgrowths were incubated in 15% (w/v in PBS) sucrose for 15 minutes and then 30% (w/v in PBS) sucrose for another 15 minutes before resuspension of the pellet in 200 µl yellow Neg-50 cryoembedding medium (Thermo Fisher, 6502Y). Samples were frozen in small cryomolds half-filled with frozen white Neg-50 cryoembedding medium (Thermo Fisher, 6502) and then surrounded with white Neg-50 immediately before freezing in a dry ice-isopentane bath. Cryosections were cut at 5 µm on a Cryostar NX50 cryostat (Epredia, 957130H) at –24ºC and air dried at room temperature before immunostaining.

Overlay culture. B2B1 cells were seeded on tissue culture plastic (6-well to 15-cm plates) at 12,500 cells/cm^2 in assay medium + 2% matrigel + 5 ng/ml EGF (Peprotech, AF-100-15) and refed every four days. On Day 6, cultures were spiked with 0.5 µM AP21967 (Takara, 635057) or 0.1% ethanol vehicle for 24 hours before cell lysis and biochemical analysis.

Laser-capture microdissection and poly(A) cDNA amplification. Rapid histologic staining, laser-capture microdissection, and poly(A) cDNA amplification were performed exactly as described previously[33, 41].

Transcriptomic profiling. 1 µg of poly(A)-amplified cDNA was labeled with Alexa Fluor 555 (Thermo Fisher, A32756) and hybridized to HumanHT-12 v4 BeadChip microarrays (Illumina, BD-901-1001) as described previously[33, 41].

Stochastic profiling analysis. BeadChip microarray fluorescence intensities were analyzed in MATLAB using StochProfMicroarrayFilt.m and StochProfAnalysis.m[41] with the following parameters: median detection threshold $P = 0.1$, maximum fold-change for reproducible detection = 5, false-discovery rate for sampling variation = 0.05, reference coefficient of variation = 0.2, and false-discovery rate for heterogeneity testing = 0.1.

Stochastic frequency matching. For the 426 genes with significant heterogeneity in B2B1 cells plus AP, we compared single-outgrowth observations with the minus-AP condition. The minus-AP data were used individually by gene to define empirical 10th and 90th percentiles for the background distribution. These percentiles were used as thresholds for the plus-AP observations to count single-outgrowth events above or below background. Taking the DE phenotype penetrance as a binomial probability ($p = 0.35$), we evaluated the probability mass function to determine how likely it was to see the observed number of events given the total number of observations: $B_{20,0.35}$. Reciprocally, we inverted the probability mass function ($B_{20,0.35}^{-1}$) to define an interval for the interquartile range of observations ([6–8] for $N = 20$) and the 90% confidence interval ([4–11] for $N = 20$). These ranges of events were used to define high-priority targets and candidates respectively.

Bulk RNA extraction and purification. Total RNA from 3D and overlay cultures was extracted with RNA STAT-60 (Tel-Test) and purified according to the manufacturer's recommendation. Total RNA from traditional 2D cultures was extracted and purified with the RNEasy Plus Mini Kit (Qiagen, 74136) according to the manufacturer's recommendation.

Bulk mRNA quantification. 0.5–1 µg total RNA from 3D or overlay cultures was treated with Turbo DNAse (Thermo Fisher, AM2238), reverse transcribed with oligo$(dT)_{24}$ (IDT) and Superscript III (Thermo Fisher, 18080044), and specific transcripts were measured by quantitative PCR as described previously[118]. Gene abundances were calibrated against purified amplicons and normalized to the geometric mean of four housekeeping genes: *GAPDH*, *GUSB*, *HINT1*, and *PRDX6*. Primer sequences are listed in Supplementary Table 7.

Intraductal xenografts. *Animals.* Female, virgin SCID/beige mice (Envigo, 186) were obtained at seven weeks of age and housed together under standard conditions. All animal work was done in compliance with ethical regulations under University of Virginia IACUC approval #3945. For the experiments using doxycycline chow, mice were given a standard rodent diet containing 625 mg/kg doxycycline (Harlan, TD.05125, IF060, HF030) before surgery, which was maintained until the end of the study.

Cell lines. Luciferase-expressing TM15c6 cells stably expressing inducible shCse1l or shGFP were cultured in DMEM medium (Gibco) plus 5% fetal bovine serum, 5 µg/ml insulin (Sigma, I1882), 1 µg/ml hydrocortisone (Sigma, H0888), 5 ng/ml EGF (Peprotech, AF-100-15), 35 µg/ml bovine pituitary extract (Gibco, 13028-014), and 50 µg/ml Gentamicin (Gibco, 15750-060) at 37°C with 1 µg/ml doxycycline added two days before inoculation.

Inoculation and imaging. Mice were anesthetized with isoflurane and the tip of each fourth mammary gland nipple was cut off with a fine scissor. Cells were suspended at a concentration of 20,000 cells/ml in growth medium plus 1 µg/ml doxycycline, and 2 µl of the cell suspension was loaded to a 30-gauge blunt needle (Hamilton, 80508) and then injected into the fourth mammary gland, with the contralateral gland receiving the paired control injection. Mouse surgical order and left-right glands assignments for experimental-control injections were randomized at the start of each experiment. Mice were imaged at 2, 5, 9, 12, 15, 18, and 22 days post-surgery on a Lago X (Spectral Instruments Imaging) after isoflurane anesthesia and intraperitoneal administration of 150 µg D-luciferin (Promega, E1605) per

gram body weight to monitor bioluminescence. Five minutes after injection, images were acquired at 2-min intervals for 30 minutes with the following settings—1 second exposure; low (2) binning; F-stop = 1.2. From Days 3–8, mice were daily administered by oral gavage 30 mg/kg lapatinib (MedChemExpress, HY-50898) dissolved in 0.5% hydroxypropyl methylcellulose in water with 0.1% Tween 80. At the terminal endpoint, mammary tumors were excised and re-imaged for high-resolution bioluminescence to quantify tumor morphometry.

Xenograft Image analysis. Bioluminescence signals (radiance, photons/second/cm^2/steradian) were quantified using Aura Imaging Software (Spectral Instruments Imaging), and the maximum steady-state luminescences were recorded for subsequent analyses. Morphological outlines of excised tumors were quantified using ImageJ.

Nucleocytoplasmic transport model. A kinetic mass-action model of three compartments (cytoplasm, nucleus, and nuclear pore) and 207 rate equations was constructed in MATLAB (R2022a) by recoding earlier efforts[60, 61] and incorporating extensive changes to parameters and network topologies. Initial conditions for B2B1 cells were determined experimentally by quantitative immunoblotting against HeLa cells, which were previously used to obtain absolute estimates[60, 61]. Complete description of the model is available in Supplementary Note 1.

Immunofluorescence. *Labeling and imaging.* Cells were plated at ~16,000 cells/cm^2 overnight on 22 x 22 mm No. 1.5 coverslips and the next day treated with 0.5 μM AP (Takara, 635057) for the indicated times where indicated. Cells were washed with 1 ml of PBS and fixed with freshly prepared 3.7% paraformaldehyde for 15 minutes at room temperature. Coverslips were washed with PBS three times for five minutes and blocked in a humid chamber for one hour at room temperature in blocking solution (1x Western Blocking reagent [Roche, 11921673001] diluted in PBS and supplemented with 0.3% Triton X-100). Primary antibodies (Supplementary Table 7) diluted in blocking solution were added overnight at room temperature. The next day, coverslips were washed with PBS three times for five minutes, and Alexa Fluor 488, 555, or 647 secondary antibodies (Thermo Fisher, A-11001, A-11008, A-21422, A-21428, A-21235, A-21244) diluted 1:200 in blocking solution were added for one hour at room temperature. Coverslips were then washed with PBS three times for five minutes, and counterstained with 0.5 μg/ml DAPI for five minutes. After two washes in PBS, coverslips were mounted with 10 μl 0.5% N-propyl gallate in 90% glycerol in 1x PBS, pH 8.0, and the edges were sealed with nail polish before imaging by widefield immunofluorescence on an Olympus BX51 microscope or a Leica STELLARIS 8 confocal microscope.

Image Analysis. Immunofluorescence images were analyzed using custom codes written in MATLAB (R2022a). Briefly, fluorescent images were background corrected using the Top-hat filtering function (imtophat), quantile-normalized, and combined by taking the geometric mean of signals to obtain a weighted measure of colocalized pixel intensities. DAPI was used to create the nuclear mask upon which colocalized signals within each nuclear mask were calculated. For cargo reporters, cells were additionally stained with 2 μg/ml wheat germ agglutinin (MP Biomedicals, 08790162) labeled with DyLight750 to create a whole-cell mask.

Proximity Ligation Assay. *Labeling and imaging.* Cells were plated at 25,000 cells/cm^2 overnight on round 12 mm No. 1.5 coverslips in a 24-well plate overnight, treated with or without 0.5 μM AP for 24 hours, and fixed–stained as with immunofluorescence up to the primary antibody step (Supplementary Table 7). Proximity ligation was performed with the Duolink In Situ Orange Starter Kit Mouse/Rabbit (Millipore Sigma, DUO92102-1KT) according to the manufacturer's recommendation. Samples were imaged in photon counting mode on a Leica STELLARIS 8 confocal microscope with a 40x objective (HC PL APO CS2 40x/1.30 OIL), 142 nm step size, 0.425 μs pixel dwell time per imaging track, 405 nm laser (1% power) excitation and 420–566 nm bandpass emission for DAPI, and 561 nm laser (0.3% power) excitation and 566–643 nm bandpass emission for Cy3. Eleven optical sections of 1 μm step size were collected from each image field and maximum-intensity projected for analysis.

Image analysis. Acquired images were processed using custom codes written in MATLAB (R2022a) to obtain the number of spots per cell. Briefly, the raw images were filtered through a rotationally symmetric Laplacian of Gaussian filter (size = 15; standard deviation = 1), and a threshold of five photons per pixel was set to identify the number of spots in each image. Each spot above the threshold was assigned to the nearest nucleus to obtain the number of spots per cell. Nuclear staining with DAPI was used to obtain a nuclear mask, nuclear objects within 100–400 μm^2 were kept for further analyses.

Chromatin immunoprecipitation (ChIP). *Sample preparation.* Overlay cultures were prepared on 15-cm plates and harvested at Day 7 with or without 0.5 µM AP treatment for the preceding 24 hours. Cells were crosslinked with 37% methanol-stabilized formaldehyde (Fisher Scientific, F79-500) at a final concentration of 1% for 10 minutes at room temperature. Crosslinking was quenched with 0.125 M Glycine for five minutes at room temperature. Cells were lysed with 300 µl lysis buffer (50 mM Tris-HCl [pH 8.0], 1% SDS, 5 mM EDTA, 10 µg/ml aprotinin, 10 µg/ml leupeptin, 1 µg/ml pepstatin, 1 mM PMSF). Chromatin was sonicated to an average size of ~200–300 bp using a Bioruptor sonicator system (Diagenode) with 4 x 20 cycles of 30 seconds ON, and 30 seconds OFF at 4ºC. After sonication, a volume of 5% chromatin was set aside for input control, and the remaining chromatin was diluted tenfold in dilution buffer (20 mM Tris-HCl [pH 8.0], 1% Triton X-100, 2 mM EDTA, 150 mM NaCl, 10 µg/ml aprotinin, 10 µg/ml leupeptin, 1 µg/ml pepstatin, 1 mM PMSF). Soluble chromatin was immuno-cleared with Protein A Plus Ultralink Resin (Thermo Scientific, 53135) for two hours at 4ºC (50 µl for 1 ml chromatin). For chromatin immunoprecipitation, 5 µg antibodies or naive IgG control was added to the precleared chromatin and incubated overnight at 4ºC. Subsequently, 50 µl of Protein A Plus Ultralink Resin was added to each ChIP reaction and incubated for four hours at 4ºC on a nutator. The pelleted beads were washed sequentially for 10 minutes on ice with 1 ml RIPA (once), 1 ml RIPA supplemented with 500 mM NaCl (three times), 1 ml LiCl buffer (10 mM Tris-HCl [pH 8.0], 1% NP-40, 1% sodium deoxycholate, 1 mM EDTA, 0.25 M LiCl) (twice), and 1 ml TE buffer (twice). The immunoprecipitated chromatin and withheld input chromatin were eluted and reverse crosslinked with elution buffer (10 mM Tris-HCl [pH 8.0], 0.5% SDS, 1 mM EDTA, 200 mM NaCl) to a final volume of 500 µl. Samples were then incubated with 100 µg/ml RNase (Qiagen, 1031301) for 30 minutes at 37ºC, followed by 200 µg/ml proteinase K (Invitrogen, 59895) for 90 minutes at 56ºC. Samples were purified by phenol-chloroform extraction and ethanol precipitation, and purified DNA was resuspended in EB buffer.

Quantitative PCR. 1 µl of purified ChIP DNA was diluted in 44 µl of H20. 4.5 µl of the diluted DNA was used for each PCR reaction. Primer sequences are listed in Supplementary Table 7. Signals from qPCR were quantified by ΔCt relative to input chromatin.

Library preparation and sequencing. Approximately 0.1–20 ng ChIP DNA was fragmented to a size range of 200 bp on a Covaris instrument for two minutes using 15 µl microTUBE-15 AFA Beads Screw-cap (Covaris 520145). Libraries were prepared with the NEBNext Ultra II DNA library preparation kit (New England Biolabs, E7645L), quantified by Qubit fluorimetry, and quality controlled on a Bioanalyzer. Samples were pooled for cBot amplification and sequenced as 75 bp paired-end reads on a NextSeq 500 (Illumina). Samples were demultiplexed with Bcl2fastq2 before analysis.

Analysis. Read quality was assessed with FastQC (version 0.11.5), and reads were aligned to the human genome (GRCh38) using Bowtie2 (version 2.2.9) with default settings. Only uniquely mapped and non-duplicated reads were selected for further analysis. Peaks were called using MACS2 (version 2.2.7.1) comparing immunoprecipitated chromatin with input chromatin using default settings.

***MIR205* quantification.** 5 ng total RNA from 3D or overlay cultures was used with the TaqMan MicroRNA Reverse Transcription Kit (Thermo Fisher, 4366596) and TaqMan MicroRNA Assays (Thermo Fisher, 4427975) for *MIR205* (Assay 000509) or *RNU6B* (Assay 001093) as a housekeeping snRNA. Abundances were quantified on a CFX96 Touch Real-Time PCR Detection System (Bio-Rad) using TaqMan Universal Master Mix II, no UNG (Thermo Fisher, 4440043) and the following thermal cycling protocol: 95ºC for 10 minutes, then 40 cycles of 95ºC for 15 seconds and 60ºC for 60 seconds.

MIR205 quantification cycles were converted to ΔCt values upon subtraction of the paired RNU6B quantification cycle, which were then converted to $\Delta\Delta$Ct values upon subtraction of the average ΔCt value for minus-AP control. Relative abundances are reported as 2-$\Delta\Delta$Ct values. Differences in $\Delta\Delta$Ct values were assessed by two- or three-way ANOVA with AP and time (when applicable) as fixed effects and biological replicate as a random effect.

REFERENCES

1. Slamon, D.J. *et al.* Human breast cancer: correlation of relapse and survival with amplification of the HER-2/neu oncogene. *Science* **235**, 177-182 (1987).
2. van de Vijver, M.J. *et al.* Neu-protein overexpression in breast cancer. Association with comedo-type ductal carcinoma in situ and limited prognostic value in stage II breast cancer. *N. Engl. J. Med.* **319**, 1239-1245 (1988).
3. Allred, D.C. *et al.* Overexpression of HER-2/neu and its relationship with other prognostic factors change during the progression of in situ to invasive breast cancer. *Hum. Pathol.* **23**, 974-979 (1992).
4. DiGiovanna, M.P. *et al.* Active signaling by HER-2/neu in a subpopulation of HER-2/neu-overexpressing ductal carcinoma in situ: clinicopathological correlates. *Cancer Res.* **62**, 6667-6673 (2002).
5. Stark, A. *et al.* HER-2/neu amplification in benign breast disease and the risk of subsequent breast cancer. *J. Clin. Oncol.* **18**, 267-274 (2000).
6. Xu, R. *et al.* Amplification of Her-2/neu gene in Her-2/neu-overexpressing and -nonexpressing breast carcinomas and their synchronous benign, premalignant, and metastatic lesions detected by FISH in archival material. *Mod. Pathol.* **15**, 116-124 (2002).
7. Park, K., Han, S., Kim, H.J., Kim, J. & Shin, E. HER2 status in pure ductal carcinoma in situ and in the intraductal and invasive components of invasive ductal carcinoma determined by fluorescence in situ hybridization and immunohistochemistry. *Histopathology* **48**, 702-707 (2006).
8. Latta, E.K., Tjan, S., Parkes, R.K. & O'Malley, F.P. The role of HER2/neu overexpression/amplification in the progression of ductal carcinoma in situ to invasive carcinoma of the breast. *Mod. Pathol.* **15**, 1318-1325 (2002).
9. Hoque, A. *et al.* Her-2/neu gene amplification in ductal carcinoma in situ of the breast. *Cancer Epidemiol Biomarkers Prev* **11**, 587-590 (2002).
10. Yu, K.D. *et al.* Different distribution of breast cancer subtypes in breast ductal carcinoma in situ (DCIS), DCIS with microinvasion, and DCIS with invasion component. *Ann. Surg. Oncol.* **18**, 1342-1348 (2011).
11. Zhang, G. *et al.* Comparison of breast ductal carcinoma in situ and ductal carcinoma in situ with microinvasion, and analysis of axillary lymph node metastasis. *Medicine (Baltimore)* **99**, e23593 (2020).
12. Okumura, Y. *et al.* Identification of biomarkers in ductal carcinoma in situ of the breast with microinvasion. *BMC Cancer* **8**, 287 (2008).
13. Lari, S.A. & Kuerer, H.M. Biological Markers in DCIS and Risk of Breast Recurrence: A Systematic Review. *J. Cancer* **2**, 232-261 (2011).
14. Yarden, Y. & Sliwkowski, M.X. Untangling the ErbB signalling network. *Nat. Rev. Mol. Cell Biol.* **2**, 127-137 (2001).
15. Zhang, X., Gureasko, J., Shen, K., Cole, P.A. & Kuriyan, J. An allosteric mechanism for activation of the kinase domain of epidermal growth factor receptor. *Cell* **125**, 1137-1149 (2006).
16. Jura, N. *et al.* Mechanism for activation of the EGF receptor catalytic domain by the juxtamembrane segment. *Cell* **137**, 1293-1307 (2009).
17. Sorkin, A. & Von Zastrow, M. Signal transduction and endocytosis: close encounters of many kinds. *Nat. Rev. Mol. Cell Biol.* **3**, 600-614 (2002).
18. Chen, M.K., Hsu, J.L. & Hung, M.C. Nuclear receptor tyrosine kinase transport and functions in cancer. *Adv. Cancer Res.* **147**, 59-107 (2020).
19. Amit, I. *et al.* A module of negative feedback regulators defines growth factor signaling. *Nat. Genet.* **39**, 503-512 (2007).
20. Shaffer, S.M. *et al.* Rare cell variability and drug-induced reprogramming as a mode of cancer drug resistance. *Nature* **546**, 431-435 (2017).
21. Dong, P. *et al.* Division of labour between Myc and G1 cyclins in cell cycle commitment and pace control. *Nat Commun* **5**, 4750 (2014).

22. Muthuswamy, S.K., Li, D., Lelievre, S., Bissell, M.J. & Brugge, J.S. ErbB2, but not ErbB1, reinitiates proliferation and induces luminal repopulation in epithelial acini. *Nat. Cell Biol.* **3**, 785-792 (2001).
23. Zhan, L., Xiang, B. & Muthuswamy, S.K. Controlled activation of ErbB1/ErbB2 heterodimers promote invasion of three-dimensional organized epithelia in an ErbB1-dependent manner: implications for progression of ErbB2-overexpressing tumors. *Cancer Res.* **66**, 5201-5208 (2006).
24. Aranda, V. *et al.* Par6-aPKC uncouples ErbB2 induced disruption of polarized epithelial organization from proliferation control. *Nat. Cell Biol.* **8**, 1235-1245 (2006).
25. Xue, B., Krishnamurthy, K., Allred, D.C. & Muthuswamy, S.K. Loss of Par3 promotes breast cancer metastasis by compromising cell-cell cohesion. *Nat. Cell Biol.* **15**, 189-200 (2013).
26. Lucs, A.V., Muller, W.J. & Muthuswamy, S.K. Shc is required for ErbB2-induced inhibition of apoptosis but is dispensable for cell proliferation and disruption of cell polarity. *Oncogene* **29**, 174-187 (2010).
27. Yu, M. *et al.* Expression profiling during mammary epithelial cell three-dimensional morphogenesis identifies PTPRO as a novel regulator of morphogenesis and ErbB2-mediated transformation. *Mol Cell Biol* **32**, 3913-3924 (2012).
28. Anczukow, O. *et al.* The splicing factor SRSF1 regulates apoptosis and proliferation to promote mammary epithelial cell transformation. *Nat. Struct. Mol. Biol.* **19**, 220-228 (2012).
29. Cabodi, S. *et al.* p130Cas is an essential transducer element in ErbB2 transformation. *FASEB J.* **24**, 3796-3808 (2010).
30. Arias-Romero, L.E. *et al.* A Rac-Pak signaling pathway is essential for ErbB2-mediated transformation of human breast epithelial cancer cells. *Oncogene* **29**, 5839-5849 (2010).
31. Bentires-Alj, M. *et al.* A role for the scaffolding adapter GAB2 in breast cancer. *Nat. Med.* **12**, 114-121 (2006).
32. Ramesh, M., Krishnan, N., Muthuswamy, S.K. & Tonks, N.K. A novel phosphatidic acid-protein-tyrosine phosphatase D2 axis is essential for ERBB2 signaling in mammary epithelial cells. *J. Biol. Chem.* **290**, 9646-9659 (2015).
33. Janes, K.A., Wang, C.C., Holmberg, K.J., Cabral, K. & Brugge, J.S. Identifying single-cell molecular programs by stochastic profiling. *Nat. Methods* **7**, 311-317 (2010).
34. Pollock, R., Giel, M., Linher, K. & Clackson, T. Regulation of endogenous gene expression with a small-molecule dimerizer. *Nat. Biotechnol.* **20**, 729-733 (2002).
35. Sun, H., Charles, C.H., Lau, L.F. & Tonks, N.K. MKP-1 (3CH134), an immediate early gene product, is a dual specificity phosphatase that dephosphorylates MAP kinase in vivo. *Cell* **75**, 487-493 (1993).
36. Emert, B.L. *et al.* Variability within rare cell states enables multiple paths toward drug resistance. *Nat. Biotechnol.* **39**, 865-876 (2021).
37. Shaffer, S.M. *et al.* Memory Sequencing Reveals Heritable Single-Cell Gene Expression Programs Associated with Distinct Cellular Behaviors. *Cell* **182**, 947-959 e917 (2020).
38. Wernet, M.F. *et al.* Stochastic spineless expression creates the retinal mosaic for colour vision. *Nature* **440**, 174-180 (2006).
39. Laslo, P. *et al.* Multilineage transcriptional priming and determination of alternate hematopoietic cell fates. *Cell* **126**, 755-766 (2006).
40. Raj, A., Rifkin, S.A., Andersen, E. & van Oudenaarden, A. Variability in gene expression underlies incomplete penetrance. *Nature* **463**, 913-918 (2010).
41. Wang, L. & Janes, K.A. Stochastic profiling of transcriptional regulatory heterogeneities in tissues, tumors and cultured cells. *Nat. Protoc.* **8**, 282-301 (2013).
42. Bajikar, S.S., Fuchs, C., Roller, A., Theis, F.J. & Janes, K.A. Parameterizing cell-to-cell regulatory heterogeneities via stochastic transcriptional profiles. *Proc. Natl. Acad. Sci. U. S. A.* **111**, E626-635 (2014).
43. Singh, S. *et al.* Pan-Cancer Drivers Are Recurrent Transcriptional Regulatory Heterogeneities in Early-Stage Luminal Breast Cancer. *Cancer Res.* **81**, 1840-1852 (2021).

44. Hajdu, T. *et al.* Comprehensive Model for Epidermal Growth Factor Receptor Ligand Binding Involving Conformational States of the Extracellular and the Kinase Domains. *Front Cell Dev Biol* **8**, 776 (2020).
45. Kaelin, W.G., Jr. Common pitfalls in preclinical cancer target validation. *Nat. Rev. Cancer* **17**, 425-440 (2017).
46. Gu, Y., Jin, S., Gao, Y., Weaver, D.T. & Alt, F.W. Ku70-deficient embryonic stem cells have increased ionizing radiosensitivity, defective DNA end-binding activity, and inability to support V(D)J recombination. *Proc. Natl. Acad. Sci. U. S. A.* **94**, 8076-8081 (1997).
47. Hurov, K.E., Cotta-Ramusino, C. & Elledge, S.J. A genetic screen identifies the Triple T complex required for DNA damage signaling and ATM and ATR stability. *Genes Dev* **24**, 1939-1950 (2010).
48. Liu, W. *et al.* BCAS2 is involved in alternative mRNA splicing in spermatogonia and the transition to meiosis. *Nat Commun* **8**, 14182 (2017).
49. Worsham, M.J. *et al.* High-resolution mapping of molecular events associated with immortalization, transformation, and progression to breast cancer in the MCF10 model. *Breast Cancer Res. Treat.* **96**, 177-186 (2006).
50. Bekpen, C. *et al.* Functional Characterization of the Morpheus Gene Family. *bioRxiv*, 116087 (2017).
51. Andrechek, E.R. *et al.* Amplification of the neu/erbB-2 oncogene in a mouse model of mammary tumorigenesis. *Proc. Natl. Acad. Sci. U. S. A.* **97**, 3444-3449 (2000).
52. Andrechek, E.R. *et al.* Gene expression profiling of neu-induced mammary tumors from transgenic mice reveals genetic and morphological similarities to ErbB2-expressing human breast cancers. *Cancer Res.* **63**, 4920-4926 (2003).
53. Dillon, R.L. *et al.* Akt1 and akt2 play distinct roles in the initiation and metastatic phases of mammary tumor progression. *Cancer Res.* **69**, 5057-5064 (2009).
54. Hu, M. *et al.* Regulation of in situ to invasive breast carcinoma transition. *Cancer Cell* **13**, 394-406 (2008).
55. Burstein, H.J., Polyak, K., Wong, J.S., Lester, S.C. & Kaelin, C.M. Ductal carcinoma in situ of the breast. *N. Engl. J. Med.* **350**, 1430-1441 (2004).
56. Behbod, F. *et al.* An intraductal human-in-mouse transplantation model mimics the subtypes of ductal carcinoma in situ. *Breast Cancer Res.* **11**, R66 (2009).
57. Bajikar, S.S. *et al.* Tumor-Suppressor Inactivation of GDF11 Occurs by Precursor Sequestration in Triple-Negative Breast Cancer. *Dev. Cell* **43**, 418-435 e413 (2017).
58. Wang, C.C., Bajikar, S.S., Jamal, L., Atkins, K.A. & Janes, K.A. A time- and matrix-dependent TGFBR3-JUND-KRT5 regulatory circuit in single breast epithelial cells and basal-like premalignancies. *Nat. Cell Biol.* **16**, 345-356 (2014).
59. Stewart, M. Molecular mechanism of the nuclear protein import cycle. *Nat. Rev. Mol. Cell Biol.* **8**, 195-208 (2007).
60. Riddick, G. & Macara, I.G. A systems analysis of importin-{alpha}-{beta} mediated nuclear protein import. *J. Cell Biol.* **168**, 1027-1038 (2005).
61. Riddick, G. & Macara, I.G. The adapter importin-alpha provides flexible control of nuclear import at the expense of efficiency. *Mol. Syst. Biol.* **3**, 118 (2007).
62. Catimel, B. *et al.* Biophysical characterization of interactions involving importin-alpha during nuclear import. *J. Biol. Chem.* **276**, 34189-34198 (2001).
63. Marfori, M., Lonhienne, T.G., Forwood, J.K. & Kobe, B. Structural basis of high-affinity nuclear localization signal interactions with importin-alpha. *Traffic* **13**, 532-548 (2012).
64. Wen, W., Meinkoth, J.L., Tsien, R.Y. & Taylor, S.S. Identification of a signal for rapid export of proteins from the nucleus. *Cell* **82**, 463-473 (1995).
65. Englmeier, L. *et al.* RanBP3 influences interactions between CRM1 and its nuclear protein export substrates. *EMBO Rep* **2**, 926-932 (2001).
66. Roux, K.J., Kim, D.I., Raida, M. & Burke, B. A promiscuous biotin ligase fusion protein identifies proximal and interacting proteins in mammalian cells. *J. Cell Biol.* **196**, 801-810 (2012).
67. Li, K. & Liu, T. Evaluation of Oncogene NUP37 as a Potential Novel Biomarker in Breast Cancer. *Front. Oncol.* **11**, 669655 (2021).

68. Wang, L., Brugge, J.S. & Janes, K.A. Intersection of FOXO- and RUNX1-mediated gene expression programs in single breast epithelial cells during morphogenesis and tumor progression. *Proc. Natl. Acad. Sci. U. S. A.* **108**, E803-812 (2011).
69. Kleinman, H.K. & Martin, G.R. Matrigel: basement membrane matrix with biological activity. *Semin. Cancer Biol.* **15**, 378-386 (2005).
70. Mellacheruvu, D. *et al.* The CRAPome: a contaminant repository for affinity purification-mass spectrometry data. *Nat. Methods* **10**, 730-736 (2013).
71. Schroeder, B., Srivatsan, S., Shaw, A., Billadeau, D. & McNiven, M.A. CIN85 phosphorylation is essential for EGFR ubiquitination and sorting into multivesicular bodies. *Mol. Biol. Cell* **23**, 3602-3611 (2012).
72. Foerster, S. *et al.* Characterization of the EGFR interactome reveals associated protein complex networks and intracellular receptor dynamics. *Proteomics* **13**, 3131-3144 (2013).
73. Haigler, H.T., McKanna, J.A. & Cohen, S. Direct visualization of the binding and internalization of a ferritin conjugate of epidermal growth factor in human carcinoma cells A-431. *J. Cell Biol.* **81**, 382-395 (1979).
74. Lin, S.Y. *et al.* Nuclear localization of EGF receptor and its potential new role as a transcription factor. *Nat. Cell Biol.* **3**, 802-808 (2001).
75. Garay, C. *et al.* Epidermal growth factor-stimulated Akt phosphorylation requires clathrin or ErbB2 but not receptor endocytosis. *Mol. Biol. Cell* **26**, 3504-3519 (2015).
76. Hsu, S.C. & Hung, M.C. Characterization of a novel tripartite nuclear localization sequence in the EGFR family. *J. Biol. Chem.* **282**, 10432-10440 (2007).
77. Madera, S. *et al.* Halting ErbB-2 isoforms retrograde transport to the nucleus as a new theragnostic approach for triple-negative breast cancer. *Cell Death Dis.* **13**, 447 (2022).
78. Lo, H.W. *et al.* Nuclear-cytoplasmic transport of EGFR involves receptor endocytosis, importin beta1 and CRM1. *J. Cell. Biochem.* **98**, 1570-1583 (2006).
79. Macara, I.G. Transport into and out of the nucleus. *Microbiol Mol Biol Rev* **65**, 570-594, table of contents (2001).
80. Soderberg, O. *et al.* Direct observation of individual endogenous protein complexes in situ by proximity ligation. *Nat. Methods* **3**, 995-1000 (2006).
81. Lo, H.W. *et al.* Nuclear interaction of EGFR and STAT3 in the activation of the iNOS/NO pathway. *Cancer Cell* **7**, 575-589 (2005).
82. Redmond, A.M., Omarjee, S., Chernukhin, I., Le Romancer, M. & Carroll, J.S. Analysis of HER2 genomic binding in breast cancer cells identifies a global role in direct gene regulation. *PLoS One* **14**, e0225180 (2019).
83. Wang, S.C. *et al.* Binding at and transactivation of the COX-2 promoter by nuclear tyrosine kinase receptor ErbB-2. *Cancer Cell* **6**, 251-261 (2004).
84. Mikula, M. *et al.* Genome-wide co-localization of active EGFR and downstream ERK pathway kinases mirrors mitogen-inducible RNA polymerase 2 genomic occupancy. *Nucleic Acids Res.* **44**, 10150-10164 (2016).
85. Wong, V.C. Nuclear EGFR and Integrator/Super Elongation Complex concurrently binds to Immediate Early Genes for gene transactivation. *J. Cancer* **9**, 108-116 (2018).
86. Ferrari, E. & Gandellini, P. Unveiling the ups and downs of miR-205 in physiology and cancer: transcriptional and post-transcriptional mechanisms. *Cell Death Dis.* **11**, 980 (2020).
87. Adachi, R. *et al.* ErbB2 down-regulates microRNA-205 in breast cancer. *Biochem Biophys Res Commun* **411**, 804-808 (2011).
88. Hasegawa, T. *et al.* ErbB2 signaling epigenetically suppresses microRNA-205 transcription via Ras/Raf/MEK/ERK pathway in breast cancer. *FEBS Open Bio* **7**, 1154-1165 (2017).
89. Zhou, C.F. *et al.* miR-205-5p inhibits human endometriosis progression by targeting ANGPT2 in endometrial stromal cells. *Stem Cell. Res. Ther.* **10**, 287 (2019).
90. Agarwal, V., Bell, G.W., Nam, J.W. & Bartel, D.P. Predicting effective microRNA target sites in mammalian mRNAs. *Elife* **4** (2015).
91. Yasuhara, N. *et al.* Triggering neural differentiation of ES cells by subtype switching of importin-alpha. *Nat. Cell Biol.* **9**, 72-79 (2007).

92. Gardner, T.S., Cantor, C.R. & Collins, J.J. Construction of a genetic toggle switch in Escherichia coli. *Nature* **403**, 339-342 (2000).
93. Kosugi, S., Hasebe, M., Tomita, M. & Yanagawa, H. Systematic identification of cell cycle-dependent yeast nucleocytoplasmic shuttling proteins by prediction of composite motifs. *Proc. Natl. Acad. Sci. U. S. A.* **106**, 10171-10176 (2009).
94. Liberzon, A. *et al.* The Molecular Signatures Database (MSigDB) hallmark gene set collection. *Cell Syst* **1**, 417-425 (2015).
95. Chambard, J.C., Lefloch, R., Pouyssegur, J. & Lenormand, P. ERK implication in cell cycle regulation. *Biochim Biophys Acta* **1773**, 1299-1310 (2007).
96. Murphy, L.O., Smith, S., Chen, R.H., Fingar, D.C. & Blenis, J. Molecular interpretation of ERK signal duration by immediate early gene products. *Nat. Cell Biol.* **4**, 556-564 (2002).
97. Boerner, J.L., Demory, M.L., Silva, C. & Parsons, S.J. Phosphorylation of Y845 on the epidermal growth factor receptor mediates binding to the mitochondrial protein cytochrome c oxidase subunit II. *Mol Cell Biol* **24**, 7059-7071 (2004).
98. Descostes, N. *et al.* Tyrosine phosphorylation of RNA polymerase II CTD is associated with antisense promoter transcription and active enhancers in mammalian cells. *Elife* **3**, e02105 (2014).
99. Harlen, K.M. *et al.* Comprehensive RNA Polymerase II Interactomes Reveal Distinct and Varied Roles for Each Phospho-CTD Residue. *Cell Rep* **15**, 2147-2158 (2016).
100. Tong, C.Y. *et al.* Detection of oncogene amplifications in medulloblastomas by comparative genomic hybridization and array-based comparative genomic hybridization. *J. Neurosurg.* **100**, 187-193 (2004).
101. Brinkmann, U., Gallo, M., Polymeropoulos, M.H. & Pastan, I. The human CAS (cellular apoptosis susceptibility) gene mapping on chromosome 20q13 is amplified in BT474 breast cancer cells and part of aberrant chromosomes in breast and colon cancer cell lines. *Genome Res.* **6**, 187-194 (1996).
102. Tian, C. *et al.* Multiplexed Thiol Reactivity Profiling for Target Discovery of Electrophilic Natural Products. *Cell Chem Biol* **24**, 1416-1427 e1415 (2017).
103. Chari, A. *et al.* Oral Selinexor-Dexamethasone for Triple-Class Refractory Multiple Myeloma. *N. Engl. J. Med.* **381**, 727-738 (2019).
104. Pahuja, K.B. *et al.* Actionable Activating Oncogenic ERBB2/HER2 Transmembrane and Juxtamembrane Domain Mutations. *Cancer Cell* **34**, 792-806 e795 (2018).
105. Waugh, M.G. & Hsuan, J.J. EGF receptors as transcription factors: ridiculous or sublime? *Nat. Cell Biol.* **3**, E209-211 (2001).
106. Wells, A. & Marti, U. Signalling shortcuts: cell-surface receptors in the nucleus? *Nat. Rev. Mol. Cell Biol.* **3**, 697-702 (2002).
107. Vilela, M. & Danuser, G. What's wrong with correlative experiments? *Nat. Cell Biol.* **13**, 1011 (2011).
108. Kinker, G.S. *et al.* Pan-cancer single-cell RNA-seq identifies recurring programs of cellular heterogeneity. *Nat. Genet.* **52**, 1208-1218 (2020).
109. Shah, N.A. & Sarkar, C.A. Robust network topologies for generating switch-like cellular responses. *PLoS Comput. Biol.* **7**, e1002085 (2011).
110. Janes, K.A. An analysis of critical factors for quantitative immunoblotting. *Sci Signal* **8**, rs2 (2015).
111. Lopacinski, A.B. *et al.* Modeling the complete kinetics of coxsackievirus B3 reveals human determinants of host-cell feedback. *Cell Syst* **12**, 304-323 e313 (2021).
112. Udeshi, N.D. *et al.* Antibodies to biotin enable large-scale detection of biotinylation sites on proteins. *Nat. Methods* **14**, 1167-1170 (2017).
113. Pereira, E.J. *et al.* Sporadic activation of an oxidative stress-dependent NRF2-p53 signaling network in breast epithelial spheroids and premalignancies. *Sci Signal* **13**, eaba4200 (2020).
114. Shin, K.J. *et al.* A single lentiviral vector platform for microRNA-based conditional RNA interference and coordinated transgene expression. *Proc. Natl. Acad. Sci. U. S. A.* **103**, 13759-13764 (2006).

115. Campeau, E. *et al.* A versatile viral system for expression and depletion of proteins in mammalian cells. *PLoS One* **4**, e6529 (2009).
116. Debnath, J., Muthuswamy, S.K. & Brugge, J.S. Morphogenesis and oncogenesis of MCF-10A mammary epithelial acini grown in three-dimensional basement membrane cultures. *Methods* **30**, 256-268 (2003).
117. Borten, M.A., Bajikar, S.S., Sasaki, N., Clevers, H. & Janes, K.A. Automated brightfield morphometry of 3D organoid populations by OrganoSeg. *Sci. Rep.* **8**, 5319 (2018).
118. Miller-Jensen, K., Janes, K.A., Brugge, J.S. & Lauffenburger, D.A. Common effector processing mediates cell-specific responses to stimuli. *Nature* **448**, 604-608 (2007).

DATA AVAILABILITY

Raw and processed microarray data are available at the Gene Expression Omnibus (GSE214455; https://www.ncbi.nlm.nih.gov/geo/query/acc.cgi?acc=GSE214455 reviewer token: qrstiycanbalxgl). Raw and processed ChIP-seq data are available at the Gene Expression Omnibus (GSE216242; https://www.ncbi.nlm.nih.gov/geo/query/acc.cgi?acc=GSE216242 reviewer token: uxmfcgayfbajjud). Proximity labeling proteomics will be deposited with the Proteomics Identification Database once the submission-publication issues with the EMBL-EBI storage system have been resolved.

CODE AVAILABILITY

The nucleocytoplasmic transport model has been deposited in the BioModels database (MODEL2210060001) and is available on GitHub (JanesLab/NucCytoShuttle).

ACKNOWLEDGMENTS

We thank Gregory Riddick for early consultation on the nucleocytoplasmic transport model, William Muller for sharing the TM15c6 cell line, Emily Farber and Suna Onengut-Gumuscu of the UVA Center for Public Health Genomics for assistance with BeadChip microarrays, Nicholas Sherman of the W.M. Keck Biomedical Mass Spectrometry Laboratory for assistance with mass spectrometry, Jun Lin for assistance with cloning, and Zhao Lai of the Greehey Children's Cancer Research Institute UT Health San Antonio for assistance with the ChIP-seq experiments. We appreciate comments from Cameron Griffiths, Wisam Fares, Piotr Przanowski, and Róża Przanowska on the manuscript figures.

This work was supported by the NCI Cancer Systems Biology Consortium (U54-CA274499 and U01-CA215794 to K.A.J.), an NCI CURE Diversity Supplement (U01-CA215794-S1 to R.A.M.), the National Cancer Institute (R50-CA265089 to L.W. and P30-CA044579 to the UVA Comprehensive Cancer Center), and the David & Lucile Packard Foundation (#2009-34710 to K.A.J.). Sequencing data was generated in the Genome Sequencing Facility, which is supported by UTHSCSA, NIH-NCI P30-CA054174 (Cancer Center Support Grant at UTHSCSA), NIH Shared Instrument grant S10-OD030311 (S10 grant to NovaSeq 6000 System), and CPRIT Core Facility Award (RP160732). The W.M. Keck Biomedical Mass Spectrometry Laboratory is funded by a grant from the UVA School of Medicine.

AUTHOR CONTRIBUTIONS

L.W. cloned and characterized B2B1 cells, performed the 10-cell profiling study, cloned genetic perturbations, and executed the proximity labeling study. B.B.P. cloned and characterized the rat-human pairs, performed and analyzed the ChIP-seq study, and analyzed immunofluorescence and PLA experiments. L.W. and B.B.P. together performed 3D experiments and in vivo experiments. R.A.M. built the nucleocytoplasmic transport model. B.B.P. and R.A.M. together performed and analyzed tandem cargo reporter experiments. K.A.J. analyzed data, edited the nucleocytoplasmic transport model, performed immunoblotting, qPCR, and PLA experiments, and drafted the manuscript. All authors edited the manuscript and secured funding to support this work

COMPETING INTERESTS

The authors declare no competing financial interests.